

# Synergistic niobium and manganese co-doping into $\text{RuO}_2$ nanocrystal enables PEM water splitting under high current

Received: 23 April 2024

Accepted: 30 April 2025

Published online: 17 May 2025



Bichen Yuan<sup>1</sup>, Qian Dang<sup>2</sup>, Hai Liu<sup>1</sup>, Marshet Getaye Sendeku<sup>3</sup>, Jian Peng<sup>4</sup>, Yameng Fan<sup>5</sup>, Liang Cai<sup>6</sup>, Aiqing Cao<sup>1</sup>, Shiyao Chen<sup>1</sup>, Hui Li<sup>2</sup>, Yun Kuang<sup>3</sup>, Fengmei Wang<sup>1</sup>✉ & Xiaoming Sun<sup>1</sup>✉

Low-cost ruthenium-based catalysts with high activity have emerged as promising alternatives to iridium-based counterparts for acidic oxygen evolution reaction (OER) in proton exchange membrane water electrolyzers (PEMWE), but the poor stability under high current density remains as a key challenge. Here, we utilize the synergistic complementary strategy of introducing earth-abundant Mn and Nb dopants in ruthenium dioxide ( $\text{RuO}_2$ ) for  $\text{Nb}_{0.1}\text{Mn}_{0.1}\text{Ru}_{0.8}\text{O}_2$  nanoparticle electrocatalyst that exhibits a low overpotential of 209 mV at  $10 \text{ mA cm}^{-2}$  and good stability of  $> 400 \text{ h}$  at  $0.2 \text{ A cm}^{-2}$  in  $0.5 \text{ M H}_2\text{SO}_4$ . Significantly, a PEMWE device fabricated with  $\text{Nb}_{0.1}\text{Mn}_{0.1}\text{Ru}_{0.8}\text{O}_2$  anode can operate continuously at least for 1000 h at  $0.5 \text{ A cm}^{-2}$  with  $59 \mu\text{V h}^{-1}$  decay rate. Operando Raman spectroscopy analysis, differential electrochemical mass spectroscopy measurements, X-ray absorption spectroscopy analysis and theoretical calculations indicate that OER reaction on  $\text{Nb}_{0.1}\text{Mn}_{0.1}\text{Ru}_{0.8}\text{O}_2$  primarily follows the adsorbate evolution mechanism with much favorable energy barrier accompanied by a locally passivated lattice oxygen mechanism (AEM-LPOM) and the co-existed Nb and Mn in  $\text{RuO}_2$  crystal lattice could not only stabilize the lattice oxygen, but also relieve the valence state fluctuation of Ru site to stabilize the catalyst during the reaction.

Hydrogen gas generated through the acidic water electrolysis technique in proton exchange membrane water electrolyzer (PEMWE) has attracted the worldwide attention due to the advantages of high gas purity under industrially relevant current density to couple with the intermittent renewable energy<sup>1–3</sup>. According to the Department of Energy (DOE), the target cost for  $\text{H}_2$  generation in PEMWE cell is US\$2 per kg of  $\text{H}_2$ <sup>4,5</sup>. And the U.S. DOE technical target for achieving an electrical efficiency of less than 48 kW h per kg of  $\text{H}_2$  by 2026<sup>6</sup>.

Furthermore, the International Renewable Energy Agency's goal of achieving an electrical efficiency (system) of less than 45 kW h per kg of  $\text{H}_2$  by 2050<sup>7</sup>. Unfortunately, the harsh acidic medium and high potential ( $> 1.4 \text{ V}$ ) of the oxygen evolution reaction (OER) usually give rise to the dissolution of active metal atoms and limited available catalysts<sup>8–10</sup>. At present, the highly valuable iridium based materials, such as  $\text{IrO}_2$ , act as the electrocatalysts in the PEMWE device for practical application, but their high cost ( $\sim$  US\$140 per gram for Ir) and

<sup>1</sup>State Key Laboratory of Chemical Resource Engineering, College of Chemistry, Beijing University of Chemical Technology, Beijing, PR China. <sup>2</sup>Beijing Advanced Innovation Center for Soft Matter Science and Engineering, Beijing University of Chemical Technology, Beijing, PR China. <sup>3</sup>Ocean Hydrogen Energy R&D Center, Research Institute of Tsinghua University in Shenzhen, Shenzhen, PR China. <sup>4</sup>Department of Mechanical and Materials Engineering, Western University, London, ON, Canada. <sup>5</sup>Institute for Superconducting and Electronic Materials, Australian Institute for Innovative Materials, University of Wollongong, Wollongong, New South Wales, Australia. <sup>6</sup>MDX Research Center for Element Strategy, International Research Frontiers Initiative, Tokyo Institute of Technology, Yokohama, Japan. ✉ e-mail: [wangfm@buct.edu.cn](mailto:wangfm@buct.edu.cn); [sunxm@mail.buct.edu.cn](mailto:sunxm@mail.buct.edu.cn)

low reserve constrains their utilization in PEMWE<sup>11</sup>. In this regard, the less expensive ruthenium-based compounds (~7.5 times cheaper than Ir<sup>11</sup>) has been recognized as an attractive alternative. However, the long-term OER stability of ruthenium-based catalysts in acid or PEM electrolyzer remains a major challenge.

By and large, the stability of ruthenium based catalysts is hindered by two factors: first, the oxidative release of lattice oxygen, which could lead to overoxidation of Ru site to soluble RuO<sub>4</sub><sup>11–14</sup> when applying a potential higher than 1.39 V; second, direct demetallization of Ru sites on the surface that trigger the collapse of the crystal structure<sup>15,16</sup>. To simultaneously improve the catalytic activity and stability of RuO<sub>2</sub> based catalysts, several methods including heterogeneous metal doping<sup>17</sup>, defect engineering<sup>18</sup>, constructing heterostructure<sup>19</sup> and controlling the morphology<sup>12</sup> have been reported. Theoretically, improving the stability of Ru based catalysts in harsh acidic conditions involves adjusting the rehearsal order of metal atoms during OER process, increasing the electron density around Ru and avoiding the oxidative release of lattice oxygen<sup>3</sup>. For instance, Qiao group proposed that the Re doping in Ru based catalyst could facilitate the withdrawal of electrons from Ru site at the on-set potential to activate OER, and then return the electrons at the higher overpotential to prevent Ru dissolution<sup>20</sup>. Peng et al. developed tungsten-ruthenium oxide heterostructures [(Ru-W) O<sub>x</sub>]<sup>21</sup> to promote the cyclic transformation of the active metal oxidation state. However, most of the electrocatalysts usually stably worked under the current density <200 mA cm<sup>-2</sup>, which is still far from the expected value for the practical application (hundreds of milliampere per centimeter square)<sup>22</sup>. Ideally, PEMWE device operated at current densities of ≥1–2 A cm<sup>-2</sup> hold promise for clean hydrogen energy production in industrial and domestic settings<sup>23</sup>. To this end, the effective design of RuO<sub>2</sub> based catalyst that resist or alleviate the demetallization of Ru site and lattice oxygen involvement under high potential in acid media is essential. Although the low ratio (<10%) of guest Nb<sup>24</sup>, Sn<sup>25</sup>, Mn<sup>26</sup> and Rh<sup>27</sup> elements were introduced into RuO<sub>2</sub> to improve the stability under current density of <300 mA cm<sup>-2</sup>, the long-term stability under higher current density of ≥500 mA cm<sup>-2</sup> for RuO<sub>2</sub>-based catalyst with smaller ratio of Ru remains underexplored and the stabilizing mechanism is not yet fully understood.

In this work, a polymetallic doped RuO<sub>2</sub> catalyst with higher atomic ratio (20%) for acidic OER is presented. Specifically, two common transition metals of Nb and Mn are introduced into RuO<sub>2</sub> (i.e., Nb<sub>x</sub>Mn<sub>0.2-x</sub>Ru<sub>0.8</sub>O<sub>2</sub>, 0 < x < 0.2) to partially substitute Ru atoms. Notably, the Nb<sub>0.1</sub>Mn<sub>0.1</sub>Ru<sub>0.8</sub>O<sub>2</sub> electrocatalyst demonstrates a low overpotential of 209 mV at the current density of 10 mA cm<sup>-2</sup>, along with good durability demonstrated by continuous operation for over 400 h at 0.2 A cm<sup>-2</sup> in 0.5 M H<sub>2</sub>SO<sub>4</sub>. Density functional theory (DFT) studies, complemented by in-situ Raman analysis, confirmed that OER reaction primarily follows the adsorbate evolution mechanism with significantly reduced energy barrier, accompanied by a locally passivated lattice oxygen mechanism (AEM-LPOM). The formation energies of Ru site and lattice oxygen could be effectively enhanced after simultaneously introducing Nb and Mn in RuO<sub>2</sub>. Ex-situ X-ray absorption spectroscopy (XAS) analysis indicates that the favorable compatibility between Mn/Nb and Ru could regulate the electron transfer to stabilize the lattice oxygen during the OER operation. As a result, the valence oscillation of Ru site in the Nb<sub>0.1</sub>Mn<sub>0.1</sub>Ru<sub>0.8</sub>O<sub>2</sub> could be relieved efficiently. In addition, a PEMWE device fabricated with Nb<sub>0.1</sub>Mn<sub>0.1</sub>Ru<sub>0.8</sub>O<sub>2</sub> anode and Pt/C cathode can be operated at 0.5 A cm<sup>-2</sup> for 1000 h with only 59 μV h<sup>-1</sup> decay rate, thus surpassing the reported electrocatalysts and demonstrating practical application. The cost for one kilogram H<sub>2</sub> generation in the PEMWE cell is estimated to be about US\$0.99 (make up the energy consumption of 6 kW h kg<sub>H<sub>2</sub></sub><sup>-1</sup>), which is much lower than the DOE target<sup>4,5</sup>. Meanwhile, the energy consumption of one PEM electrolyzer is calculated as 43.69 kW h kg<sub>H<sub>2</sub></sub><sup>-1</sup>, which is less than 45 kW h kg<sub>H<sub>2</sub></sub><sup>-1</sup>. Overall, this work not only provides a feasible

approach to stabilize the RuO<sub>2</sub> crystal for acidic OER, but effectively decreases the cost of catalyst by introducing relatively earth-abundant transition metals to substitute Ru.

## Results and discussion

### Synthesis and characterizations of Nb<sub>x</sub>Mn<sub>0.2-x</sub>Ru<sub>0.8</sub>O<sub>2</sub>

To effectively improve the stability of RuO<sub>2</sub> based catalyst for acidic OER through doping heterogeneous elements, the following rationale was considered. First, the radius of the doped metal ion should be close to that of Ru<sup>4+</sup> according to Hume-Rothery rules<sup>28,29</sup>. Second, the electronegativity difference between the target metal ion to be introduced and Ru site in the solid solution should not be too large to prevent the formation of impurities. Third, the Ru valence state should be regulated by the doped metal atoms and its oxidation state should not significantly increase during the acidic OER process. Considering the aforementioned guiding principles, the slightly larger radius of Nb<sup>5+</sup> than Ru<sup>4+</sup> (0.64 Å versus 0.62 Å) and our previous result<sup>24</sup> were taken as solid foundation to select Nb as one of the incorporated elements. The less electronegativity of Nb<sup>4+</sup> (χ<sub>Nb4+</sub> = 1.690) than that of Ru<sup>4+</sup> (χ<sub>Ru4+</sub> = 1.848<sup>24,30</sup>) could increase the electron density on the Ru site through weakening the covalency between Ru and O, and hence, eliminate the excessive oxidation of Ru site. In addition, the third element of Mn with same valence state and slightly smaller radius to Ru<sup>4+</sup> (0.58 Å for Mn<sup>3+</sup> and 0.53 Å for Mn<sup>4+</sup>) is selected to balance the charge and release the lattice stress in Nb doped RuO<sub>2</sub> for further improving activity and stability.

Thus, we prepare Mn and Nb co-doped RuO<sub>2</sub> (Fig. 1a) by utilizing the sol-gel method (see details in the Experimental Procedures). The Ru to metals (Nb and Mn) ratio is maintained at 0.8 to 0.2 (samples designated as N<sub>x</sub>M<sub>0.2-x</sub>RO) while the Nb and Mn ratio is tuned through varying the ratio of metal precursor i.e., Nb<sub>x</sub>Mn<sub>0.2-x</sub>Ru<sub>0.8</sub>O<sub>2</sub> (x = 0.05, 0.07, 0.1, 0.13, and 0.15). As comparisons, the Nb<sub>0.2</sub>Ru<sub>0.8</sub>O<sub>2</sub> (NRO), Mn<sub>0.2</sub>Ru<sub>0.8</sub>O<sub>2</sub> (MRO) and home-made RuO<sub>2</sub> (HM-RuO<sub>2</sub>) samples were also prepared via the same method. The elemental ratios of Ru, Nb, and Mn in the as-prepared N<sub>x</sub>M<sub>0.2-x</sub>RO samples were confirmed by energy-dispersive X-ray spectroscopy (EDS), and the products show almost same ratio with that of the precursor used (Supplementary Figs. 1–7 and Supplementary Table 1). The scanning electron microscopy (SEM) images in Supplementary Fig. 8 reveal the as-prepared samples exhibit nanoparticle morphology with the size of 20–30 nm. X-ray diffraction (XRD) patterns collected from the various samples (Fig. 1b) showed that as-prepared N<sub>x</sub>M<sub>0.2-x</sub>RO possesses the same crystal phase as rutile RuO<sub>2</sub> (JCPDS file no. 43-1027) without any evidence for impurity from Nb<sub>2</sub>O<sub>5</sub> and MnO<sub>2</sub>, suggesting the Nb and Mn substitution of Ru in RuO<sub>2</sub> lattice. Since the radius of Nb<sup>4+</sup> is larger than that of Ru<sup>4+</sup>, the diffraction peaks corresponding to (110) and (101) planes shift toward smaller degree with the increase in Nb content. While, the Mn substitution drive the diffraction peaks to the original degree, especially for the (101) and (110) plane<sup>24,31</sup>. When the doping ratio of Nb and Mn is 1:1 (N<sub>0.1</sub>M<sub>0.1</sub>RO), the XRD peak positions are basically consistent with those of home-made RuO<sub>2</sub> due to the synergistic and complementary characteristics of Nb and Mn elements. From the high-resolution transmission electron microscopy (HRTEM, Fig. 1c) image and the corresponding selected area electron diffraction patterns (Supplementary Figs. 9, 10), the N<sub>0.1</sub>M<sub>0.1</sub>RO and rutile RuO<sub>2</sub> samples exhibit similar lattice spacing of 0.318 nm for (110) plane. As shown in Fig. 1d, the TEM image and corresponding elemental mappings verified the uniform distribution of Ru, Mn, and Nb throughout the samples. Raman spectra conducted on N<sub>0.1</sub>M<sub>0.1</sub>RO (Fig. 1e) demonstrate three peak around 511, 623, and 691 cm<sup>-1</sup>, which can be assigned to E<sub>g</sub>, A<sub>1g</sub>, and B<sub>2g</sub> modes, respectively, of rutile RuO<sub>2</sub><sup>32</sup>. Notably, the absence of vibration modes for Nb and Mn based oxide species further rule out the existence of other oxide impurities.

Next, the surface electronic properties and the chemical coordination environment of N<sub>x</sub>M<sub>0.2-x</sub>RO samples were investigated using

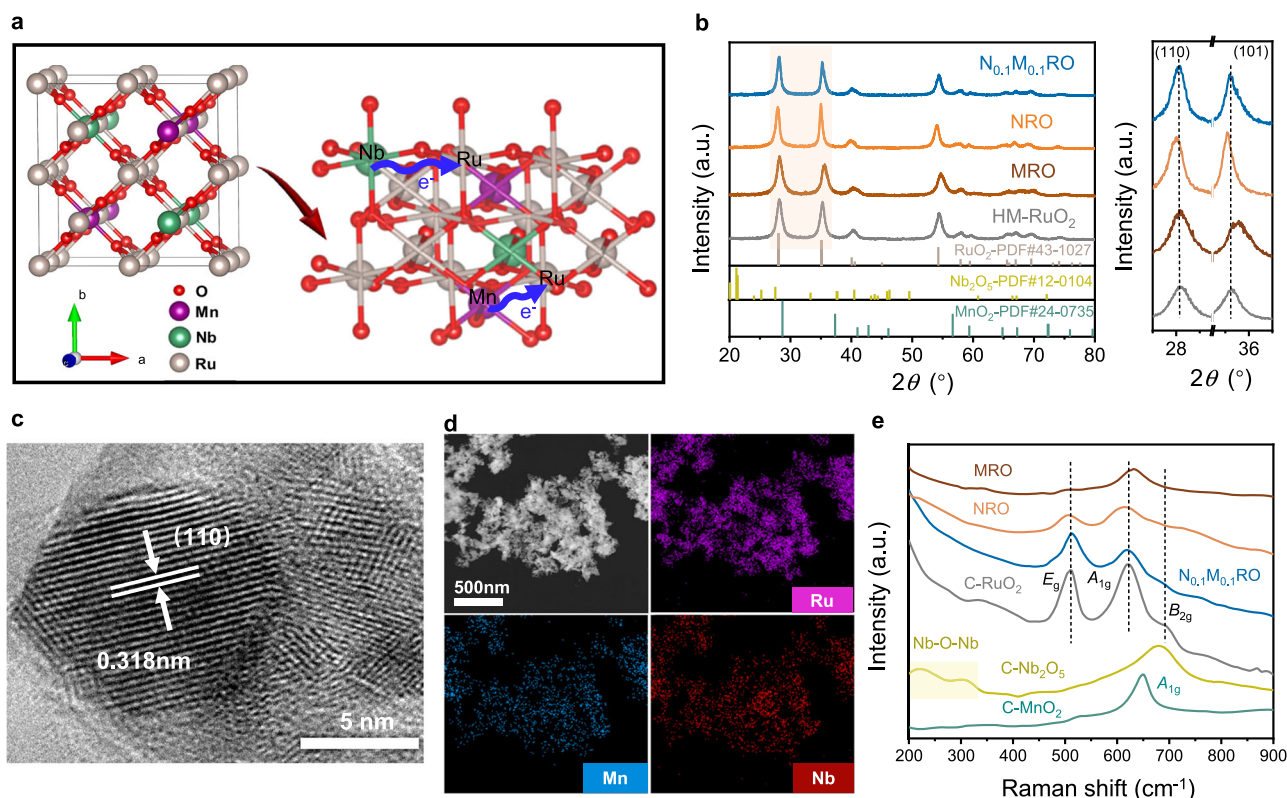


**Fig. 1 | Structural and compositional characterizations of  $N_xM_{0.2-x}RO$  samples.** **a** Schematic of the Nb and Mn co-doped rutile  $RuO_2$  crystal. **b** XRD patterns (left) of the as-synthesized  $N_{0.1}M_{0.1}RO$ , HM- $RuO_2$ , NRO, and MRO samples. The XRD peaks at 28° and 35° for (110) and (101) planes are magnified (right). **c** HRTEM image of

$N_{0.1}M_{0.1}RO$ . **d** TEM image and corresponding EDS elemental mappings of  $N_{0.1}M_{0.1}RO$ . **e** Raman spectra of  $N_xM_{0.2-x}RO$ , compared with those of C- $RuO_2$ , C- $MnO_2$ , and C- $Nb_2O_5$  powder.

X-ray photoelectron spectroscopy (XPS) and synchrotron XAS. High resolution Ru 3d XPS spectra exhibit two peaks located at 282.00 and 286.20 eV corresponding to Ru 3d<sub>5/2</sub> and Ru 3d<sub>3/2</sub> (Fig. 2a), which display a slight shift to the lower binding energy by about 0.4 eV compared with that of HM- $RuO_2$ <sup>11</sup>. This result indicates the valence state of Ru for  $N_{0.1}M_{0.1}RO$  sample is below +4. Meanwhile, we can clearly see that doping Nb or Mn ion can reduce the valence state of Ru in  $N_xM_{0.2-x}RO$ . The co-doping of Nb and Mn in  $RuO_2$  will further give rise to the lower valence state of Ru. From this XPS analysis, the ratio of  $Ru^{3+}/Ru^{4+}$  is higher in the  $N_{0.1}M_{0.1}RO$  sample (0.67) compared to that in the NRO (0.43) and MRO (0.54), indicating a higher abundance of  $Ru^{3+}$  species<sup>33</sup>. Additionally, the Nb 3d XPS analysis (Supplementary Fig. 11a) of the  $N_{0.1}M_{0.1}RO$  sample exhibits the peak centered at 206.30 eV, for Nb 3d<sub>5/2</sub>, which is 0.7 eV lower than that of Nb<sup>5+</sup> (207 eV) and 1.1 eV higher than that of Nb<sup>4+</sup> (205.2 eV)<sup>34</sup>. Hence, the oxidation state of Nb in  $N_{0.1}M_{0.1}RO$  is between +4 and +5. Meanwhile, the XPS analysis of Mn in the as-synthesized samples (Supplementary Fig. 11b) shows that the Mn 2p<sub>3/2</sub> peak in  $N_{0.1}M_{0.1}RO$  is positioned at the same binding energy as that of Mn<sub>2</sub>O<sub>3</sub>, suggesting that the valence state of Mn is close to +3. Whereas the oxidation state of Mn in MRO samples is close to +4. These results revealed the balanced and decreased valence states of Nb and Mn in the  $N_{0.1}M_{0.1}RO$  crystal compared to the single-element doping ones (i.e., NRO and MRO samples).

To study the chemical coordination environment after introducing the Nb and Mn ions into rutile  $RuO_2$ , we conducted synchrotron XAS. The X-ray absorption near-edge structure (XANES) spectra at Ru K-edge (Fig. 2b) presents similar spectral pattern to that of standard C- $RuO_2$  with a slight shift to the lower energy. Accordingly, the valence states of Ru and Mn in various samples are calculated based on their absorption energy ( $E_0$ ) which was obtained from the first maximum in

the first-order derivative as the electron vacancy, respectively<sup>35,36</sup> (Supplementary Fig. 12a). The average oxidation state of Ru in  $N_{0.1}M_{0.1}RO$  (ca. 3.79) is lower than that in  $RuO_2$ , which is consistent with XPS analysis. The XANES at the Mn K-edge (Fig. 2c) show that the absorption energy for  $N_{0.1}M_{0.1}RO$  sample is located between Mn<sub>2</sub>O<sub>3</sub> and MnO<sub>2</sub> standards, indicating the average oxidation state of Mn in  $N_{0.1}M_{0.1}RO$  and MRO is between +3 and +4. Specifically, the oxidation state of Mn in  $N_{0.1}M_{0.1}RO$  and MRO is calculated to be +3.25 and +3.52, respectively (Supplementary Fig. 12b). We anticipate that the co-existence of Nb and Mn ions in rutile  $RuO_2$  could simultaneously reduce the initial valence state of Ru by donating electrons through M-O-Ru that emanate from the electronegativity differences ( $\chi_{Mn^{3+}} = 1.73$ ,  $\chi_{Nb^{4+}} = 1.690$ , and  $\chi_{Ru^{4+}} = 1.848$ ). Furthermore, extended X-ray absorption fine structure (EXAFS) spectra of Ru K-edge and Mn K-edge reveal the coordination structures of  $N_{0.1}M_{0.1}RO$ , MRO, with C- $RuO_2$ , C- $MnO_2$ ,  $RuCl_3$ , and Ru foil as the references (Fig. 2d). Two main peaks of -1.44 and -2.91 Å corresponding to the first Ru-O shell and the next nearest Ru-Ru/Mn/Nb shell in Ru K-edge EXAFS are clearly observed. The length of the first shell in  $N_{0.1}M_{0.1}RO$  is almost the same as that in C- $RuO_2$  due to the balanced strain and charge. Notably, the first Mn-O shell in Mn K-edge EXAFS spectra of  $N_{0.1}M_{0.1}RO$  exhibit the same peak position with the first Ru-O shell in Ru K-edge EXAFS, and next M-M shells in Mn K-edge EXAFS spectra for  $N_{0.1}M_{0.1}RO$  are obviously different from Mn K-edge EXAFS spectra of MnO<sub>2</sub> and Mn<sub>2</sub>O<sub>3</sub>. These results indicate the substitution of Ru by Mn could partially isolate Ru sites and possess a coordination environment similar to that of the Ru site in  $N_{0.1}M_{0.1}RO$  without Mn-O-Mn coordination. Accordingly, the EXAFS wavelet transformed (WT) analysis in Fig. 2f, g reveals that the intensity maxima corresponding to the nearest neighbor Ru-O/Mn-O is located at  $-4.7 \text{ \AA}^{-1}$ , which is similar to

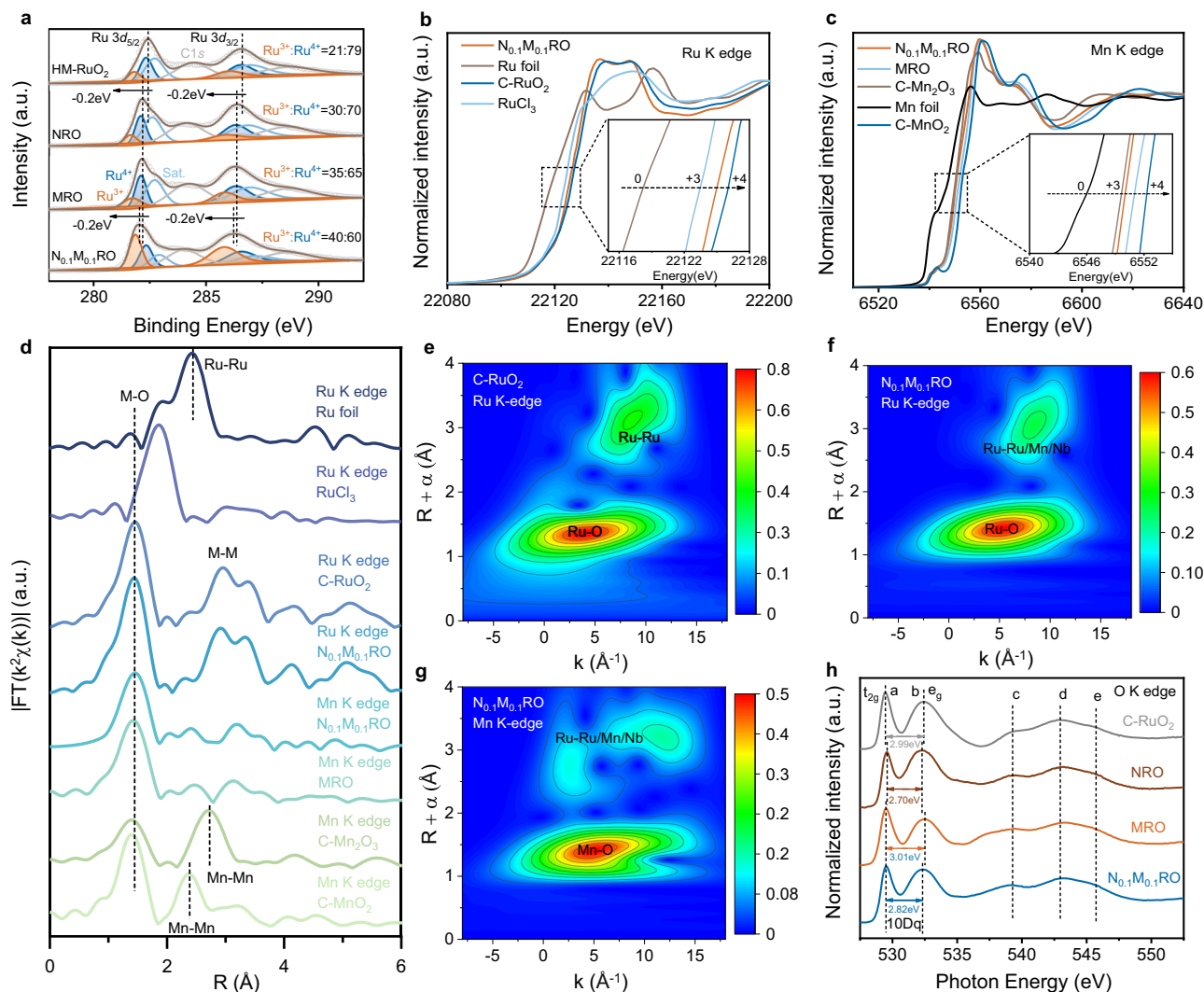


**Fig. 2 | XPS and XAS characterizations for  $N_{0.1}M_{0.1}RO$  samples. a** Ru 3d XPS spectra of  $N_{0.1}M_{0.1}RO$ , NRO, MRO, and HM-RuO<sub>2</sub>. **b** Ru K-edge spectra of Ru foil, RuCl<sub>3</sub>, and  $N_{0.1}M_{0.1}RO$  along with pure RuO<sub>2</sub>. **c** Mn K-edge spectra of Mn foil, Mn<sub>2</sub>O<sub>3</sub>,  $N_{0.1}M_{0.1}RO$ , and MRO along with pure MnO<sub>2</sub>. **d** Fourier-transformed Ru/Mn K-edge EXAFS in R spaces of  $N_{0.1}M_{0.1}RO$ , MRO, compared with Ru foil, RuCl<sub>3</sub>, RuO<sub>2</sub>,

MnO<sub>2</sub>, and Mn<sub>2</sub>O<sub>3</sub> references. **e** Ru K-edge WT-EXAFS for C-RuO<sub>2</sub>. **f** Ru K-edge WT-EXAFS for  $N_{0.1}M_{0.1}RO$ . **g** Mn K-edge WT-EXAFS for  $N_{0.1}M_{0.1}RO$ . **h** O K-edge XAS spectra collected from  $N_{0.1}M_{0.1}RO$ , NRO, MRO, compared with that of C-RuO<sub>2</sub> reference.

that of C-RuO<sub>2</sub> (Fig. 2e). In addition, the Nb K-edge EXAFS spectra of the first Nb-O shell in  $N_{0.1}M_{0.1}RO$  also exhibit a similar coordination environment with that of Ru in  $N_{0.1}M_{0.1}RO$ , further excluding the formation of Nb-O-Nb coordination and Nb<sub>2</sub>O<sub>5</sub> impurities (Supplementary Figs. 13 and 14 and Supplementary Table 2).

The O K-edge XANES spectra collected from various samples are then analyzed (Fig. 2h). Five peaks of “a–e” at the O K-edge that arise from the dipole transitions from 1s to unoccupied 2p states of O site are observed. And the fine features presented are due to the transition between the hybridized states of O 2p and Ru 4d or Ru 5sp in the octahedral ( $O_h$ ) crystal field with rutile structure sharing similar spectra pattern: “a” peak at 529.5 eV ( $t_{2g}$ ) and “b” peak at 532.4 eV ( $e_g$ ) are transition from O 1s to unoccupied  $O_{2p}$ - $M_{4d}$  hybridized states of split  $t_{2g}$  and  $e_g$ ; while “c–e” peaks (539.2, 543.1, and 545.8 eV) are transitions from O 1s to O 2p-Ru 5sp hybridized bands<sup>37,38</sup>. Accordingly, the fission energy value<sup>39</sup> of 10Dq between  $t_{2g}$  and  $e_g$  in various samples are calculated (Supplementary Table 3). Meanwhile, the normalized relative intensity analysis of “a” and “b” peaks (i.e.,  $I_{eg}/I_{t2g}$ )<sup>40</sup> could further provide insight into the local structural and electronic state of Ru. The calculated  $I_{eg}/I_{t2g}$  ratios for NRO (~1.03) is larger than that for C-RuO<sub>2</sub>

(~0.84). In addition, we can find that if Mn ions are introduced, the change in the fission energy values for MRO (~3.01) is slightly increased and the  $I_{eg}/I_{t2g}$  ratio is slightly decreased (~0.81) compared to those of C-RuO<sub>2</sub>, which demonstrate the inverse trend with those of NRO. Due to the synergistic effect of guest Nb and Mn elements,  $N_{0.1}M_{0.1}RO$  possesses the lower 10 Dq value (~2.82) and the higher  $I_{eg}/I_{t2g}$  ratio (~0.94) than C-RuO<sub>2</sub>. This suggests that the electrons on the  $t_{2g}$  state of Ru 4d in  $N_{0.1}M_{0.1}RO$  is increased, reducing the dipole transition probability from the O 1s and valence state of Ru<sup>3+/4+</sup>. In other words, the smaller 10Dq value or higher  $I_{eg}/I_{t2g}$ , the more Ru<sup>n+</sup> ( $3 < n < 4$ ) ions in the sample. As a result, the co-doping of guest Nb and Mn in  $N_{0.1}M_{0.1}RO$  demonstrate the moderate fission energy and  $I_{eg}/I_{t2g}$  ratio values, leading to the negligible change in crystal symmetry. These results are well consistent with XPS analysis results. The O 1s XPS spectra of NRO sample (Supplementary Fig. 15) demonstrate a peak located at 530.87 eV corresponding to lattice oxygen, and this peak is higher than that for C-RuO<sub>2</sub> sample. However, Mn incorporation effectively regulated its electronic structure (XPS peak shift to the lower binding energy), which is mainly due to the smaller electronegativity of Mn<sup>3+</sup> compared to Nb<sup>5+</sup> and Ru<sup>4+</sup> ( $\chi_{Mn^{3+}} = 1.73$  versus

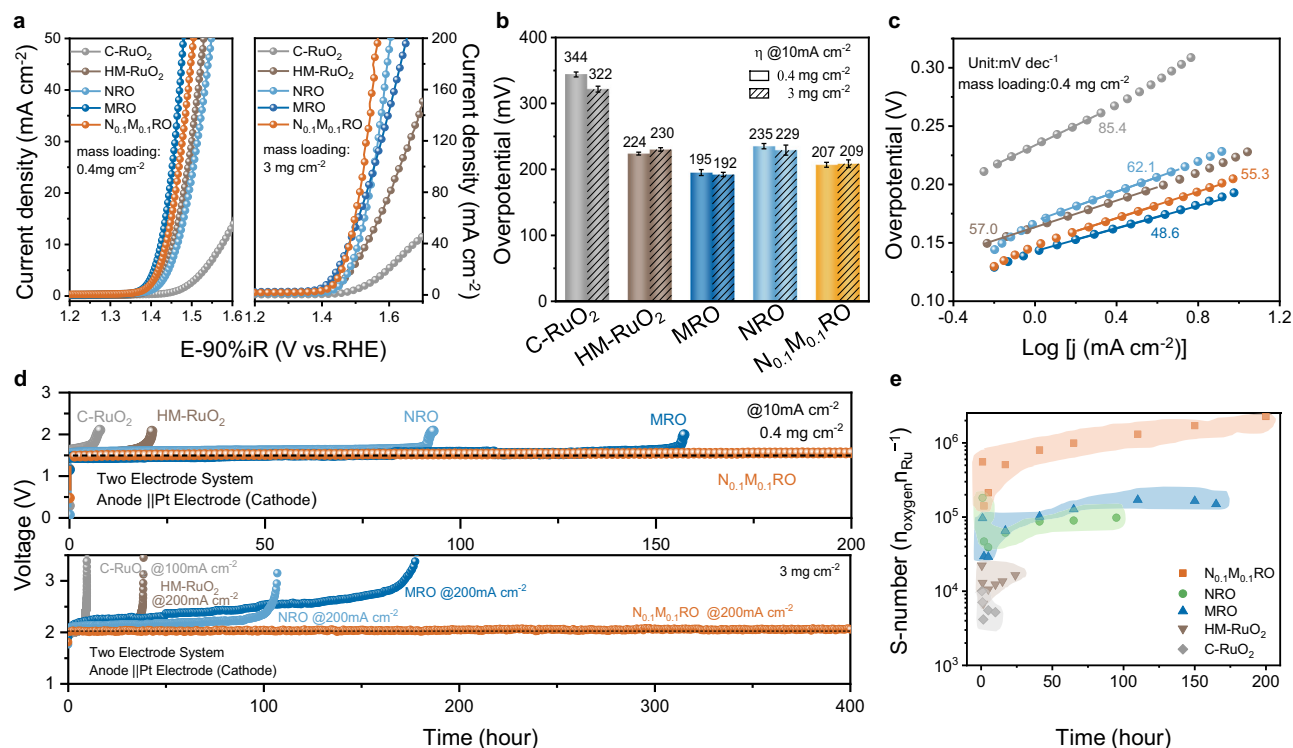


**Fig. 3 | Electrocatalytic properties of  $N_xM_{0.2-x}RO$  catalysts towards OER in 0.5 M  $H_2SO_4$  electrolyte. a, b** Polarization curves with 90%  $iR$ -correction (a) of  $N_{0.1}M_{0.1}RO$  (with  $R_s = 4.47 \pm 0.4 \Omega$  at  $0.4 \text{ mg cm}^{-2}$  loading and  $3.15 \pm 0.4 \Omega$  at  $3 \text{ mg cm}^{-2}$  loading), NRO (with  $R_s = 5.16 \pm 0.5 \Omega$  at  $0.4 \text{ mg cm}^{-2}$  loading and  $3.14 \pm 0.5 \Omega$  at  $3 \text{ mg cm}^{-2}$  loading), MRO (with  $R_s = 4.82 \pm 0.4 \Omega$  at  $0.4 \text{ mg cm}^{-2}$  loading and  $3.70 \pm 0.4 \Omega$  at  $3 \text{ mg cm}^{-2}$  loading), home-made  $RuO_2$  (with  $R_s = 5.02 \pm 0.5 \Omega$  at  $0.4 \text{ mg cm}^{-2}$  loading and  $3.41 \pm 0.5 \Omega$  at  $3 \text{ mg cm}^{-2}$  loading), and C- $RuO_2$  (with  $R_s = 4.71 \pm 0.6 \Omega$  at  $0.4 \text{ mg cm}^{-2}$  loading and  $3.70 \pm 0.6 \Omega$  at  $3 \text{ mg cm}^{-2}$  loading) at a scan rate of  $5 \text{ mV s}^{-1}$  and the corresponding overpotential values (b). Note, the

non- $iR$  corrected voltammograms and Nyquist plots of all the catalysts mentioned above are shown in Supplementary Figs. 16 and 17, the method for fabricating the electrodes is detailed in the Methods section. c The corresponding Tafel plots collected from  $N_xM_{0.2-x}RO$ , HM- $RuO_2$ , and C- $RuO_2$ . d Comparison of chronopotentiometry responses of  $N_{0.1}M_{0.1}RO$ , NRO, MRO, HM- $RuO_2$ , and C- $RuO_2$  electrodes at current densities of 10, 100 or 200  $\text{mA cm}^{-2}$  (Top,  $0.4 \text{ mg cm}^{-2}$  catalyst loaded on Ti mesh; Bottom,  $3 \text{ mg cm}^{-2}$  catalyst loaded on the carbon paper). e S-number values collected from  $N_xM_{0.2-x}RO$ , HM- $RuO_2$ , and C- $RuO_2$  electrode during the stability test in the top of the (d).

$\chi_{Nb5+} = 1.862$ , and  $\chi_{Ru4+} = 1.848$ )<sup>30,42</sup>. Therefore, the position of the lattice oxygen peak of the synthesized  $N_{0.1}M_{0.1}RO$  sample lies between the NRO and MRO. Combined with the previous XAS and XPS analysis, we can conclude that the  $N_{0.1}M_{0.1}RO$  sample possess an unchanged rutile crystal structure similar with C- $RuO_2$ , but Ru site exists in its lower valence state.

### Electrochemical acidic OER property of $N_xM_{0.2-x}RO$ in three-electrode system

The OER catalytic activities of  $N_{0.1}M_{0.1}RO$  catalysts are evaluated in a traditional three-electrode system using  $O_2$  saturated  $0.5 \text{ M } H_2SO_4$  (see Methods for the details). The working electrodes were prepared with different mass loadings of  $0.4$  and  $3 \text{ mg cm}^{-2}$ . As the comparison, the C- $RuO_2$ , NRO, MRO, and HM- $RuO_2$  samples were studied under the same condition. The linear scanning voltammetry (LSV) curves after  $iR$  correction in Fig. 3a and the corresponding overpotential values are presented in Fig. 3b. The  $N_{0.1}M_{0.1}RO$ , C- $RuO_2$ , HM- $RuO_2$ , MRO, and NRO electrodes with mass loading of  $0.4 \text{ mg cm}^{-2}$  require a catalytic overpotential of 207, 344, 224, 195, and 235 mV, respectively, to deliver a current density of  $10 \text{ mA cm}^{-2}$ . When the mass loading was increased to  $3 \text{ mg cm}^{-2}$ , there is no obvious difference in the overpotential values under the same current density (Fig. 3a, b and Supplementary Figs. 16 and 17). The introduction of Mn can improve the activity of  $RuO_2$  more easily than Nb. We also conduct a comparative analysis of activity and stability of  $N_xM_{0.2-x}RO$  ( $x = 0.05, 0.07, 0.1, 0.13$ , and  $0.15$ ) samples with different Nb/Mn doping ratios (Supplementary Fig. 18). The  $N_{0.1}M_{0.1}RO$  catalyst exhibits significantly enhanced activity, Tafel slope, and stability compared with others due to the synergistic effect

of Nb and Mn with optimum doping amount. Specifically, the  $N_{0.1}M_{0.1}RO$  sample also shows the highest mass activity of  $127.0 \text{ A g}_{Ru}^{-1}$  at  $1.48 \text{ V vs. RHE}$  (Supplementary Fig. 19 and Table 4), which is 2.12, 1.94, and 22.13 folds higher than that of NRO, HM- $RuO_2$ , and C- $RuO_2$ , respectively. The  $N_{0.1}M_{0.1}RO$  electrode exhibits a lower Tafel slope value of  $55.3 \text{ mV dec}^{-1}$  (Fig. 3c) compared to the NRO ( $62.1 \text{ mV dec}^{-1}$ ), HM- $RuO_2$  ( $57.0 \text{ mV dec}^{-1}$ ), and C- $RuO_2$  ( $85.4 \text{ mV dec}^{-1}$ ) electrodes, aligning with recently reported findings<sup>20,24</sup>. This suggests that moderate Nb and Mn doping plays a critical role in promoting OER kinetics and accelerating electron transfer.

The durability of  $N_{0.1}M_{0.1}RO$  catalyst is also an important parameter for evaluating the performance of catalysts. Figure 3d (top) shows the chronopotentiometry curve of the catalysts loaded on a Ti mesh with a loading mass of  $0.4 \text{ mg}_{catalyst} \text{ cm}^{-2}$  at  $10 \text{ mA cm}^{-2}$ . It can be seen that there is no change in the potential during a continuous 200-h testing. While the C- $RuO_2$ , HM- $RuO_2$ , NRO, and MRO electrodes showed a rapid decay in activity within 8, 21, 92, and 157 h testing, respectively. To better evaluate the stability of catalysts, the inductively coupled plasma mass spectrometry (ICP-MS) analysis were correspondingly used to monitor the dissolution of Ru, Mn, and Nb ions during the long-term stability test<sup>43</sup>. As shown in Fig. 3e and Supplementary Table 5, the dissolved Ru, Nb and Mn ions from  $N_{0.1}M_{0.1}RO$  electrode were only  $0.33 \text{ wt}_{Ru}\%$ ,  $0.25 \text{ wt}_{Nb}\%$ , and  $0.37 \text{ wt}_{Mn}\%$  within 200-h reaction, respectively. As the comparison, the dissolution of Ru from the C- $RuO_2$  and HM- $RuO_2$  electrodes is  $6.0 \text{ wt}_{Ru}\%$  and  $4.5 \text{ wt}_{Ru}\%$  within 10-h and 24-h reaction, respectively. These findings confirm the significantly prohibited Ru dissolution after co-doping the Mn and Nb elements. The higher concentration of Ru ions in the electrolytes in

which NRO (3.7 wt<sub>Ru</sub>% for 95-h reaction) and MRO (4.0 wt<sub>Ru</sub>% for 165-h reaction) electrodes were measured also reveal the synergistic and complementary effect of doped Mn and Nb ions to boost the stability of  $\text{N}_{0.1}\text{M}_{0.1}\text{RO}$  electrode. Furthermore, the stability number (S-number) of  $\text{N}_{0.1}\text{M}_{0.1}\text{RO}$  catalyst is determined as  $2.27 \times 10^6$ , much higher than those of MRO ( $1.49 \times 10^5$ ) and NRO ( $9.80 \times 10^4$ ) electrocatalysts, and also well-placed among reported Ru-based and Ir-based catalysts (Supplementary Table 6).

Catalyst stability at high potential is also crucial for employing an acidic OER electrode at industrial scale. In this regard, we investigate and compare the stability of the as-synthesized catalysts by chronopotentiometry (CP) measurements under high current densities (100 and 200  $\text{mA cm}^{-2}$ , Fig. 3d). The dramatically decay is observed within 10-h testing on the C-RuO<sub>2</sub> (1.03 V) electrodes under the current density of 100  $\text{mA cm}^{-2}$  due to the severe leach of the Ru sites. Notably, the  $\text{N}_{0.1}\text{M}_{0.1}\text{RO}$  electrode is operated at a current density of 200  $\text{mA cm}^{-2}$  for 400 h with low attenuation rate of 0.08  $\text{mV h}^{-1}$  (Supplementary Table 7), outperforming the HM-RuO<sub>2</sub> (920 mV decay within 38.4 h), NRO (874 mV decay within 106.8 h) and MRO (1778 mV decay within 171.6 h) electrodes. This shows that the two elements incorporated via the sol-gel method play synergistic role to improve the activity (via Mn introduction) and stability (by using Nb).

Then, we thoroughly compared the stability of  $\text{N}_{0.1}\text{M}_{0.1}\text{RO}$  catalyst with other recently reported Ru-based catalysts utilizing decay rate and operation time as comparison metrics. Generally, operation at higher current density could lead to more severe decay in the catalyst performance. Supplementary Table 7 illustrates that the  $\text{N}_{0.1}\text{M}_{0.1}\text{RO}$

electrode exhibits superior performance compared to the current benchmark sample tested in 0.5 M H<sub>2</sub>SO<sub>4</sub>. The stability of  $\text{N}_{0.1}\text{M}_{0.1}\text{RO}$  under working conditions was verified by Raman characterization technique. As depicted in Supplementary Fig. 20, the crystal structure remains almost unchanged during continuous acidic OER catalysis over 400 h as evidenced by the Raman vibrational displacement below 700  $\text{cm}^{-1}$  at the 200  $\text{mA cm}^{-2}$ . Further, the electrolyte after stability testing was analyzed using inductively coupled plasma mass spectrometry (ICP-MS). As shown in Supplementary Table 8, the Ru dissolution rate in the electrolyte when the  $\text{N}_{0.1}\text{M}_{0.1}\text{RO}$  electrode operated under 200  $\text{mA cm}^{-2}$  for 400 h is only 0.020%, which is significantly lower than the values for C-RuO<sub>2</sub> operated under 100  $\text{mA cm}^{-2}$  for 9.6 h (2.98%), MRO (0.073%) and NRO (0.090%) operated at 200  $\text{mA cm}^{-2}$  for 171.6 h and 106.8 h, respectively. This dramatically reduced Ru dissolution rate indicates that the co-doping with Nb and Mn can effectively prevent the collapse and inactivation of the RuO<sub>2</sub> crystal structure.

### Mechanism explanation for OER activity and stability of $\text{N}_{0.1}\text{M}_{0.1}\text{RO}$ catalyst

The adsorption evolution mechanism (AEM) and the lattice oxygen mechanism (LOM) were considered based on the previous studies<sup>15,44,45</sup> (Supplementary Fig. 21). To experimentally probe the OER mechanism, operando Raman spectrum analysis was performed on  $\text{N}_{0.1}\text{M}_{0.1}\text{RO}$  catalyst in 0.1 M HClO<sub>4</sub> (Supplementary Fig. 22). Figure 4a shows the operando Raman spectra of  $\text{N}_{0.1}\text{M}_{0.1}\text{RO}$  catalyst under different potential ranging from open circuit potential (OCP) to 1.8 V. Notably, a

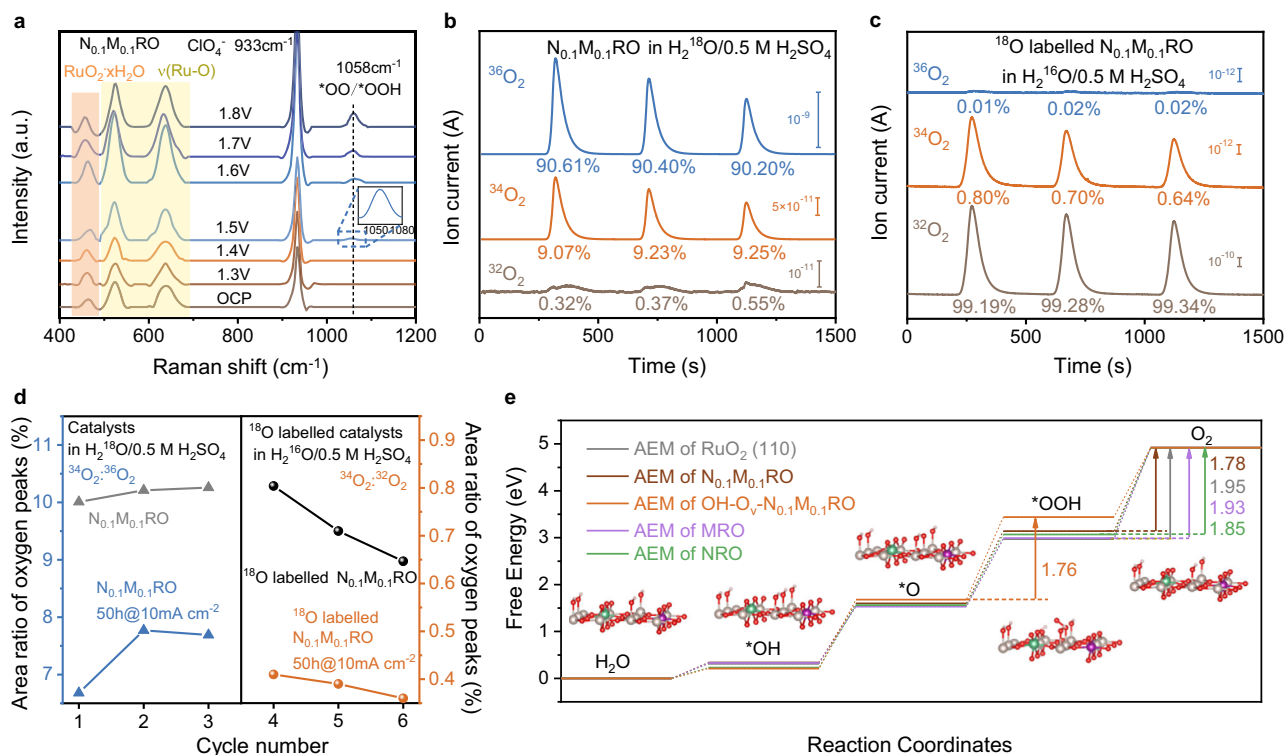


**Fig. 4 | Operando experimental studies and theoretical calculations for acidic OER activity and stability of  $\text{N}_{0.1}\text{M}_{0.1}\text{RO}$  catalyst.** **a** In-situ Raman measurement on  $\text{N}_{0.1}\text{M}_{0.1}\text{RO}$  catalyst loaded on the carbon paper substrate. The tests were carried out at different potentials (from 1.3 to 1.8 V vs. RHE without  $iR$  correction) in 0.1 M HClO<sub>4</sub>. **b** DEMS signals of  $^{32}\text{O}_2$ ,  $^{34}\text{O}_2$ , and  $^{36}\text{O}_2$  from the gaseous products for  $\text{N}_{0.1}\text{M}_{0.1}\text{RO}$  catalysts in 0.5 M H<sub>2</sub>SO<sub>4</sub> electrolyte prepared in H<sub>2</sub><sup>18</sup>O. The DEMS response was collected during three CV cycles in the potential range of 1.14 to 1.69 V vs. RHE at a scan rate of 5  $\text{mV s}^{-1}$ . **c** DEMS signals of  $^{32}\text{O}_2$ ,  $^{34}\text{O}_2$ , and  $^{36}\text{O}_2$  from the gaseous products for  $^{18}\text{O}$ -labelled  $\text{N}_{0.1}\text{M}_{0.1}\text{RO}$  catalysts in H<sub>2</sub><sup>16</sup>O/0.5 M H<sub>2</sub>SO<sub>4</sub>

electrolyte in the potential range of 1.14 to 1.79 V versus RHE at a scan rate of 5  $\text{mV s}^{-1}$ , which is repeated three cycles. **d** The comparison of mass spectroscopy peak area ratio of  $^{34}\text{O}_2/^{36}\text{O}_2$  for  $\text{N}_{0.1}\text{M}_{0.1}\text{RO}$  and  $\text{N}_{0.1}\text{M}_{0.1}\text{RO}$  50 h@10  $\text{mA cm}^{-2}$  catalysts in H<sub>2</sub><sup>18</sup>O aqueous H<sub>2</sub>SO<sub>4</sub> electrolyte (left) and  $^{34}\text{O}_2/^{32}\text{O}_2$  for  $^{18}\text{O}$  labelled  $\text{N}_{0.1}\text{M}_{0.1}\text{RO}$  and  $\text{N}_{0.1}\text{M}_{0.1}\text{RO}$  50 h@10  $\text{mA cm}^{-2}$  catalysts in H<sub>2</sub><sup>16</sup>O aqueous H<sub>2</sub>SO<sub>4</sub> electrolyte (right). **e** The free energy diagram for AEM path on the surface of OH-O<sub>v</sub>- $\text{N}_{0.1}\text{M}_{0.1}\text{RO}$  (110) and  $\text{N}_{0.1}\text{M}_{0.1}\text{RO}$  (110) model, compared with RuO<sub>2</sub> (110), MRO (110), and NRO (110) models, at 0 V. The energy barrier of the rate determining step for the different reaction steps are labeled by arrows.

peak around  $1058\text{ cm}^{-1}$  assigned for the stretching vibration of  $\ast\text{OO}/\ast\text{OOH}$  species is observed at potential above  $1.5\text{ V}$  vs RHE. This peak emerges as the potential reaches the OER region ( $\geq 1.5\text{ V}$ ), suggesting the generation of  $\ast\text{OO}/\ast\text{OOH}$  intermediate. Note that the Raman peaks at  $933\text{ cm}^{-1}$  and  $460\text{ cm}^{-1}$  are the typical vibration peak of  $\text{ClO}_4^-$  and  $\text{RuO}_2 \cdot x\text{H}_2\text{O}$ <sup>46</sup>, respectively. This result suggests that the OER process on  $\text{N}_{0.1}\text{M}_{0.1}\text{RO}$  catalyst mainly follows the AEM mechanism<sup>47,48</sup>. Next, we further conducted operando differential electrochemical mass spectrometry (DEMS) measurements via isotope  $^{18}\text{O}$ -labelling method<sup>49</sup> (Fig. 4b, c and Supplementary Fig. 23). First, the  $\text{N}_{0.1}\text{M}_{0.1}\text{RO}$  was labeled with  $^{18}\text{O}$  by performing OER through three CV-cycle operations in  $\text{H}_2^{18}\text{O}/0.5\text{ M H}_2\text{SO}_4$  (Supplementary Fig. 24). If the lattice oxygen is involved,  $^{18}\text{O}$  would be labeled on the catalyst surface. Figure 4b shows that the  $^{36}\text{O}_2$  signal of  $>90\%$  is dominated with trace  $^{32}\text{O}_2$  of  $0.3\text{--}0.5\%$  and  $^{34}\text{O}_2$  of  $\sim 9\%$ , and the ratio of  $^{34}\text{O}_2$  versus  $^{36}\text{O}_2$  signals remains relatively constant ( $\sim 10\%$ ) over three cycles in  $\text{H}_2^{18}\text{O}/0.5\text{ M H}_2\text{SO}_4$  (Fig. 4d, left). As controls, the C-RuO<sub>2</sub> and MRO catalysts were also measured under the same condition (Supplementary Figs. 25–27) and the ratio of  $^{34}\text{O}_2$  versus  $^{36}\text{O}_2$  signal for C-RuO<sub>2</sub> was kept  $\sim 10\%$ , which is similar to that obtained with  $\text{N}_{0.1}\text{M}_{0.1}\text{RO}$  catalyst and lower than that ( $>10\%$ ) for MRO catalyst. Then, we tested the same electrodes (i.e.,  $^{18}\text{O}$ -labelled  $\text{N}_{0.1}\text{M}_{0.1}\text{RO}$ ) in  $\text{H}_2^{16}\text{O}/0.5\text{ M H}_2\text{SO}_4$  after carefully washing it by  $\text{H}_2^{16}\text{O}$  (Fig. 4c). The highest  $^{32}\text{O}_2$  signal of  $>99\%$  was detected from  $^{18}\text{O}$ -labelled  $\text{N}_{0.1}\text{M}_{0.1}\text{RO}$ , along with the unchanged  $^{34}\text{O}_2$ :  $^{32}\text{O}_2$  ratio of  $0.65\% - 0.80\%$  (Fig. 4d, right) and negligible  $^{36}\text{O}_2$ . It can be observed that the  $^{34}\text{O}_2$ :  $^{32}\text{O}_2$  ratio gradually decreases in  $\text{H}_2^{16}\text{O}/0.5\text{ M H}_2\text{SO}_4$  electrolyte after three CV cycles. Meanwhile, the  $^{34}\text{O}_2$ :  $^{32}\text{O}_2$  ratio for  $^{18}\text{O}$ -labelled C-RuO<sub>2</sub> is higher than that for  $^{18}\text{O}$ -labelled  $\text{N}_{0.1}\text{M}_{0.1}\text{RO}$  under the same CV test (Supplementary Fig. 27). These results imply that the lattice oxygen would participate in OER in the beginning, and then the OER process mainly proceeds through the AEM pathway. To confirm this point, the  $\text{N}_{0.1}\text{M}_{0.1}\text{RO}$  catalyst after 50-h durability test (i.e.,  $\text{N}_{0.1}\text{M}_{0.1}\text{RO}$  50 h@10 mA cm<sup>-2</sup>) was collected and further be measured through the isotope  $^{18}\text{O}$ -labelling process. As shown in Supplementary Fig. 28, the ratio of  $^{34}\text{O}_2$  versus  $^{32}\text{O}_2$  signals for  $^{18}\text{O}$ -labelled  $\text{N}_{0.1}\text{M}_{0.1}\text{RO}$  50 h@10 mA cm<sup>-2</sup> remained at  $\sim 0.4\%$  in  $\text{H}_2^{16}\text{O}/0.5\text{ M H}_2\text{SO}_4$ , much lower than that for the fresh  $\text{N}_{0.1}\text{M}_{0.1}\text{RO}$  catalyst. These findings indicate that the lattice oxygen in the  $\text{N}_{0.1}\text{M}_{0.1}\text{RO}$  catalyst would be gradually passivated, resulting in the suppression of the LOM pathway and subsequently enhancing the stability of OER (Fig. 4d).

DFT calculations were then preformed to theoretically understand the effect of Mn and Nb substitution in RuO<sub>2</sub> on the OER activity. The  $\text{N}_{0.1}\text{M}_{0.1}\text{RO}$  model is built on the RuO<sub>2</sub> (110) structure, with partial Ru sites substituted by Nb and Mn atoms (Supplementary Fig. 29), and the most stable one as the potential active surface. Based on the XPS and XAS analysis results, the OH- $\text{N}_{0.1}\text{M}_{0.1}\text{RO}$  model and OH-O<sub>v</sub>- $\text{N}_{0.1}\text{M}_{0.1}\text{RO}$  model with oxygen vacancy were also constructed to simulate the catalyst after reaction. The post-screened RuO<sub>2</sub> (110), MRO (110), and NRO (110) surfaces were also simulated and calculated for comparison (Supplementary Figs. 29–33). As shown in Supplementary Figs. 34 and 35, the energy barrier for  $\text{N}_{0.1}\text{M}_{0.1}\text{RO}$  at  $U = 0\text{ V}$  is higher for LOM (3.90 eV) than AEM (1.78 eV), which indicates that the AEM is more favorable. The theoretical results, in-situ Raman analysis and isotope-labeled DEMS could reveal that  $\text{N}_{0.1}\text{M}_{0.1}\text{RO}$  mainly follows the AEM pathway. The free energy diagram of the AEM path on  $\text{N}_{0.1}\text{M}_{0.1}\text{RO}$  model (Fig. 4e) shows that the  $\ast\text{OOH} \rightarrow \text{O}_2$  step is the rate-determining step. Meanwhile, the obtained energy barrier of 1.78 eV for  $\text{N}_{0.1}\text{M}_{0.1}\text{RO}$  model is smallest among all models (1.95 eV for RuO<sub>2</sub>, 1.93 eV for MRO and 1.85 eV for NRO). These results reveal that the synergistic effect of Nb and Mn substitution in  $\text{N}_{0.1}\text{M}_{0.1}\text{RO}$  endows higher catalytic activity towards OER, which is also confirmed by the higher adsorption energy (3.14 eV) for the key intermediate  $\ast\text{OOH}$  on  $\text{N}_{0.1}\text{M}_{0.1}\text{RO}$  to release O<sub>2</sub> molecular (Supplementary Table 9). When the surface of the  $\text{N}_{0.1}\text{M}_{0.1}\text{RO}$  model is covered by OH species in OH-

$\text{N}_{0.1}\text{M}_{0.1}\text{RO}$  model, the energy barrier is 1.73 eV under AEM pathway, which is comparable to that of LOM pathway (1.97 eV) (Supplementary Fig. 36). This theoretical result suggests that when the OH adsorbs on the  $\text{N}_{0.1}\text{M}_{0.1}\text{RO}$  catalyst surface along with the start of reaction, the OER process could follow the LOM pathway to contribute to the formation of oxygen vacancies in the catalyst, which could be further confirmed through the following ex-situ XAS analysis and the change in the coordination number around Ru. The same calculations conducted on the OH-O<sub>v</sub>- $\text{N}_{0.1}\text{M}_{0.1}\text{RO}$  (Supplementary Fig. 37) reveal that the energy barrier of LOM (3.20 eV) is much higher than that of AEM (1.76 eV), indicating that the local lattice oxygen could be finally passivated (namely, AEM-LPOM) and stabilized in the crystal structure containing OH and oxygen vacancies. Afterwards, the OER process on OH-O<sub>v</sub>- $\text{N}_{0.1}\text{M}_{0.1}\text{RO}$  would follow the AEM pathway and the catalyst presents robust stability within long-term stability testing. Although it is generally considered that Mn is unstable in acid, the higher demetallation energy values of Mn in both  $\text{N}_{0.1}\text{M}_{0.1}\text{RO}$  (3.9 eV) and OH-O<sub>v</sub>- $\text{N}_{0.1}\text{M}_{0.1}\text{RO}$  models (3.8 eV) than that in the MnO<sub>2</sub> (2.6 eV) were achieved to verify the improved stability of Mn sites during the OER process (Supplementary Figs. 38 and 39). Besides, based on the ion electronegativity values ( $\chi_{\text{Mn}^{3+}} = 1.73$ ,  $\chi_{\text{Nb}^{4+}} = 1.690$ , and  $\chi_{\text{Ru}^{4+}} = 1.848$ ), the lower electronegativity of Nb<sup>4+</sup> and Mn<sup>3+</sup> compared to that of Ru<sup>4+</sup> suggests that the Nb and Mn sites are more oxyphilic<sup>50,51</sup>, which is consistent with the XAS analysis results with higher coordination number around Nb and Mn. The Bader charge analysis of the  $\text{N}_{0.1}\text{M}_{0.1}\text{RO}$  and OH-O<sub>v</sub>- $\text{N}_{0.1}\text{M}_{0.1}\text{RO}$  models (Supplementary Fig. 40) shows that both Nb and Mn sites are more likely to donate electrons to oxygen atoms, thereby preventing the formation of soluble RuO<sub>4</sub> and enhancing structural stability during the OER. The highest energy values for Ru demetalization (2.16 eV) and O loss (2.50 eV) from the OH-O<sub>v</sub>- $\text{N}_{0.1}\text{M}_{0.1}\text{RO}$  model are achieved on OH-O<sub>v</sub>- $\text{N}_{0.1}\text{M}_{0.1}\text{RO}$  (Supplementary Figs. 41 and 42), further providing evidence for its robust stability. In short, co-doping of Nb- and Mn- not only improves the activity of the catalyst, but also enhances its stability during OER catalysis.

### Ex-situ XAS analysis of $\text{N}_{0.1}\text{M}_{0.1}\text{RO}$ during acidic OER process

To further understand the role of co-doped Nb and Mn in RuO<sub>2</sub> for enhancing acidic OER performance and stability, we conducted ex-situ XAS characterizations under different current densities and operation time. Two identical  $\text{N}_{0.1}\text{M}_{0.1}\text{RO}$  electrodes were utilized for evaluating them at different operation time: the first electrode was tested at a small current density of  $10\text{ mA cm}^{-2}$  for 50 h (denoted as  $\text{N}_{0.1}\text{M}_{0.1}\text{RO}$  50 h@10 mA cm<sup>-2</sup>) while the second one was evaluated at a higher current density of  $200\text{ mA cm}^{-2}$  for 150 h (denoted as  $\text{N}_{0.1}\text{M}_{0.1}\text{RO}$  150 h@200 mA cm<sup>-2</sup>). Then, the XANES and EXAFS spectra of these two electrodes were recorded. As shown in Fig. 5a, the XANES spectra at Ru K-edge collected on both of  $\text{N}_{0.1}\text{M}_{0.1}\text{RO}$  electrodes show a very similar spectral pattern to that of the original one with slight shift in absorption energies and decreased white line intensity. When  $\text{N}_{0.1}\text{M}_{0.1}\text{RO}$  electrode was operated at  $10\text{ mA cm}^{-2}$  for 50 h, the absorption energy for  $\text{N}_{0.1}\text{M}_{0.1}\text{RO}$  50 h@10 mA cm<sup>-2</sup> is red-shifted with a lower average oxidation state of Ru. Whereas a slightly decrease on the oxidation state is recorded for the  $\text{N}_{0.1}\text{M}_{0.1}\text{RO}$  150 h@200 mA cm<sup>-2</sup> compared with that for  $\text{N}_{0.1}\text{M}_{0.1}\text{RO}$  50 h@10 mA cm<sup>-2</sup> electrode. Accordingly, the average oxidation state of Ru for  $\text{N}_{0.1}\text{M}_{0.1}\text{RO}$  is calculated to be +3.79 for  $\text{N}_{0.1}\text{M}_{0.1}\text{RO}$ , +3.32 for  $\text{N}_{0.1}\text{M}_{0.1}\text{RO}$  50 h@10 mA cm<sup>-2</sup>, and +3.26 for  $\text{N}_{0.1}\text{M}_{0.1}\text{RO}$  150 h@200 mA cm<sup>-2</sup>, confirming that the average oxidation state of Ru exhibits a decreasing trend after the long-term stability measurement. This is in accord to the trend observed in Nb-doped RuO<sub>2</sub><sup>24</sup>.

In contrast, the Mn K-edge XANES spectra (Fig. 5b) show a different trend with the average oxidation state of Mn, i.e., +3.25 for fresh  $\text{N}_{0.1}\text{M}_{0.1}\text{RO}$ , +3.89 for  $\text{N}_{0.1}\text{M}_{0.1}\text{RO}$  50 h@10 mA cm<sup>-2</sup> and +3.45 for  $\text{N}_{0.1}\text{M}_{0.1}\text{RO}$  150 h@200 mA cm<sup>-2</sup>, although a similar spectral pattern to that original one is also presented. Notably, the average oxidation state

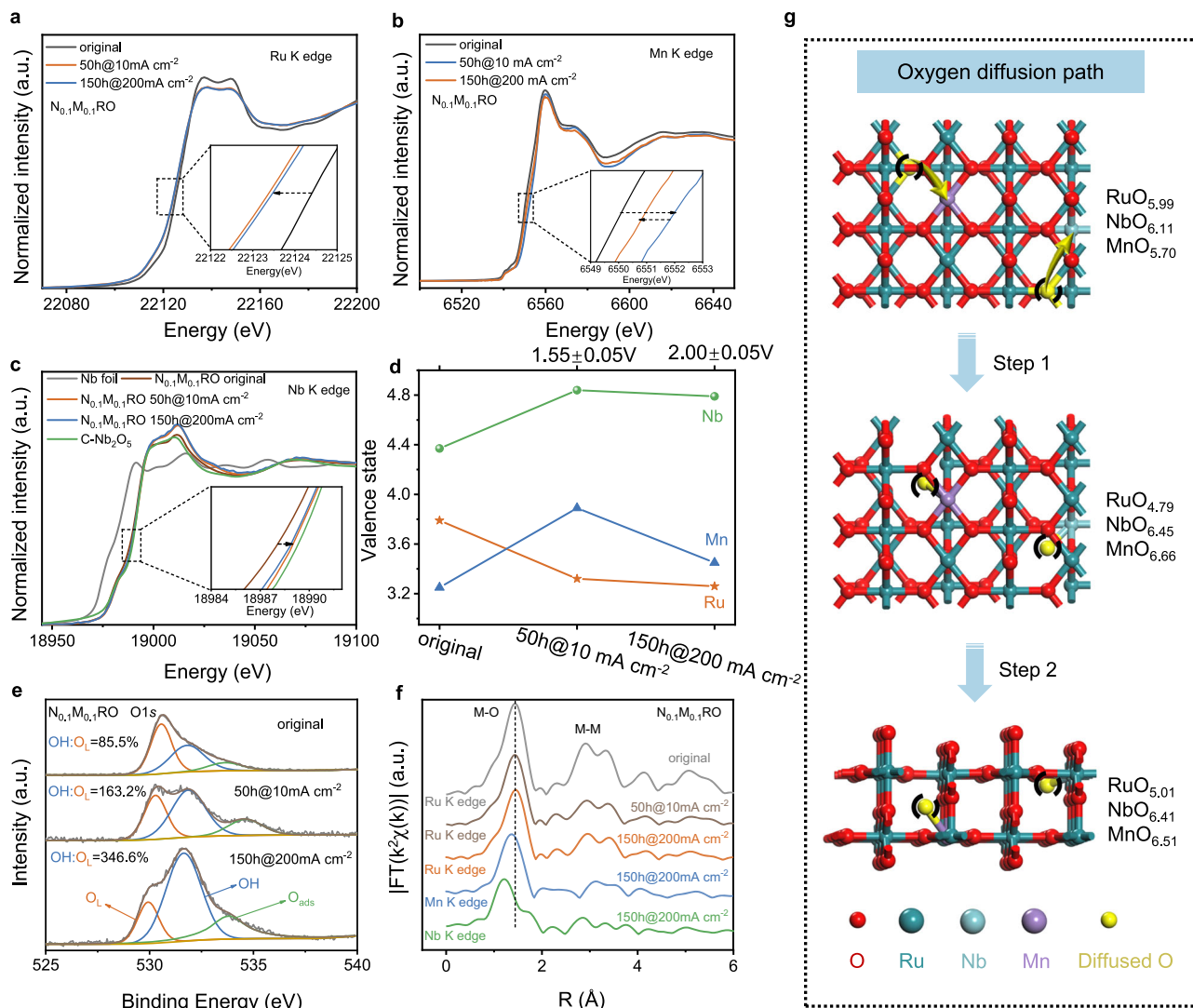


**Fig. 5 | Ex-situ XAS and XPS characterizations to understand the stability of N<sub>0.1</sub>M<sub>0.1</sub>RO catalyst for acidic OER.** **a–c** Ru K-edge (**a**), Mn K-edge (**b**), and Nb K-edge (**c**) XANES spectra of N<sub>0.1</sub>M<sub>0.1</sub>RO after different operation times under different current densities in 0.5 M H<sub>2</sub>SO<sub>4</sub>. Insets, extended image of the selected area. **d** The valence state evolution of Ru, Nb, and Mn elements during the acidic OER measurement. **e** O 1s XPS spectra of original N<sub>0.1</sub>M<sub>0.1</sub>RO, N<sub>0.1</sub>M<sub>0.1</sub>RO

50 h@10 mA cm<sup>-2</sup> and N<sub>0.1</sub>M<sub>0.1</sub>RO 150 h@200 mA cm<sup>-2</sup> in 0.5 M H<sub>2</sub>SO<sub>4</sub>.

**f** Corresponding Fourier-transformed Ru K-edge EXAFS profiles in R spaces for N<sub>0.1</sub>M<sub>0.1</sub>RO and Fourier-transformed EXAFS profile comparison in Ru, Mn, and Nb K-edges of N<sub>0.1</sub>M<sub>0.1</sub>RO after 150 h durability tests under 200 mA cm<sup>-2</sup>. **g** The illustration of the oxygen diffusion in the N<sub>0.1</sub>M<sub>0.1</sub>RO based on the EXAFS analysis results.

of Nb shows a slight increase from +4.37 to +4.84 at the beginning and finally restored to +4.79 after the long-term stability test (Fig. 5c, d and Supplementary Fig. 43). Meanwhile, fresh N<sub>0.1</sub>M<sub>0.1</sub>RO and spent over N<sub>0.1</sub>M<sub>0.1</sub>RO 100 h@200 mA cm<sup>-2</sup> catalyst were characterized using Low-magnification TEM (Supplementary Fig. 44). These further corroborates with the XPS analysis where the Ru 3d XPS spectra of N<sub>0.1</sub>M<sub>0.1</sub>RO 50 h@10 mA cm<sup>-2</sup> sample (Supplementary Fig. 45) exhibit a notable red-shift (by about 0.3 eV) in its 3d<sub>5/2</sub> or 3d<sub>3/2</sub> peak<sup>41,52</sup>. It can be noted that the valence state of Ru in N<sub>0.1</sub>M<sub>0.1</sub>RO 150 h@200 mA cm<sup>-2</sup> is still lower than the original one with the obviously red-shift in binding energy. As a comparison, the Nb-3d XPS spectra (Supplementary Fig. 46a) show that the 3d<sub>5/2</sub> peak shifts to higher binding energy by 0.48 eV for N<sub>0.1</sub>M<sub>0.1</sub>RO 50 h@10 mA cm<sup>-2</sup>, but this shift is less significant (0.07 eV) in N<sub>0.1</sub>M<sub>0.1</sub>RO 150 h@200 mA cm<sup>-2</sup>. The Mn 2p XPS analysis (Supplementary Fig. 46b) also demonstrates the same trend as shown in ex-situ XANES spectra. In addition, the M-O peak for N<sub>0.1</sub>M<sub>0.1</sub>RO 50 h@10 mA cm<sup>-2</sup> and N<sub>0.1</sub>M<sub>0.1</sub>RO 150 h@200 mA cm<sup>-2</sup> samples in the O 1s XPS spectra shifted by -0.27 and 0.62 eV respectively to lower binding energy, compared to that of original N<sub>0.1</sub>M<sub>0.1</sub>RO

(Fig. 5e). Moreover, the ratio of OH to M-O peak gradually increases from 85.5% for fresh N<sub>0.1</sub>M<sub>0.1</sub>RO to higher values for tested samples, i.e., 163.2% for N<sub>0.1</sub>M<sub>0.1</sub>RO 50 h@10 mA cm<sup>-2</sup> and 346.6% for N<sub>0.1</sub>M<sub>0.1</sub>RO 150 h@200 mA cm<sup>-2</sup>. We speculate that the catalyst surface would gradually hydrogenate after a period of reaction, thus stabilizing the Ru site with lower oxidation state. Overall, these observations indicate the incorporation of both Mn and Nb could effectively relieve the valence oscillation of Ru to stabilize the catalyst during the acidic OER.

The EXAFS profiles in R space of N<sub>0.1</sub>M<sub>0.1</sub>RO 50 h@10 mA cm<sup>-2</sup> further show the slightly longer Ru-O bond and decreased intensity (Fig. 5f and Supplementary Fig. 47), suggesting the reduced number of coordinated oxygens (Supplementary Table 2). The coordination number (CN) of the first Ru-O shell demonstrates a decreased value of 4.79 at 10 mA cm<sup>-2</sup> for 50 h, and finally stabilized to 5.01 at 200 mA cm<sup>-2</sup> for 150 h. We speculate that the first step of the reaction may be the diffusion of oxygen around RuO<sub>6</sub> to NbO<sub>6</sub>/MnO<sub>6</sub>, which can be seen from the decrease in the coordination number (CN) of the first shell Ru-O and the increase of the coordination number (CN) of the first shell Nb-O and Mn-O. After a period of reaction, RuO<sub>x</sub>, NbO<sub>x</sub>, and

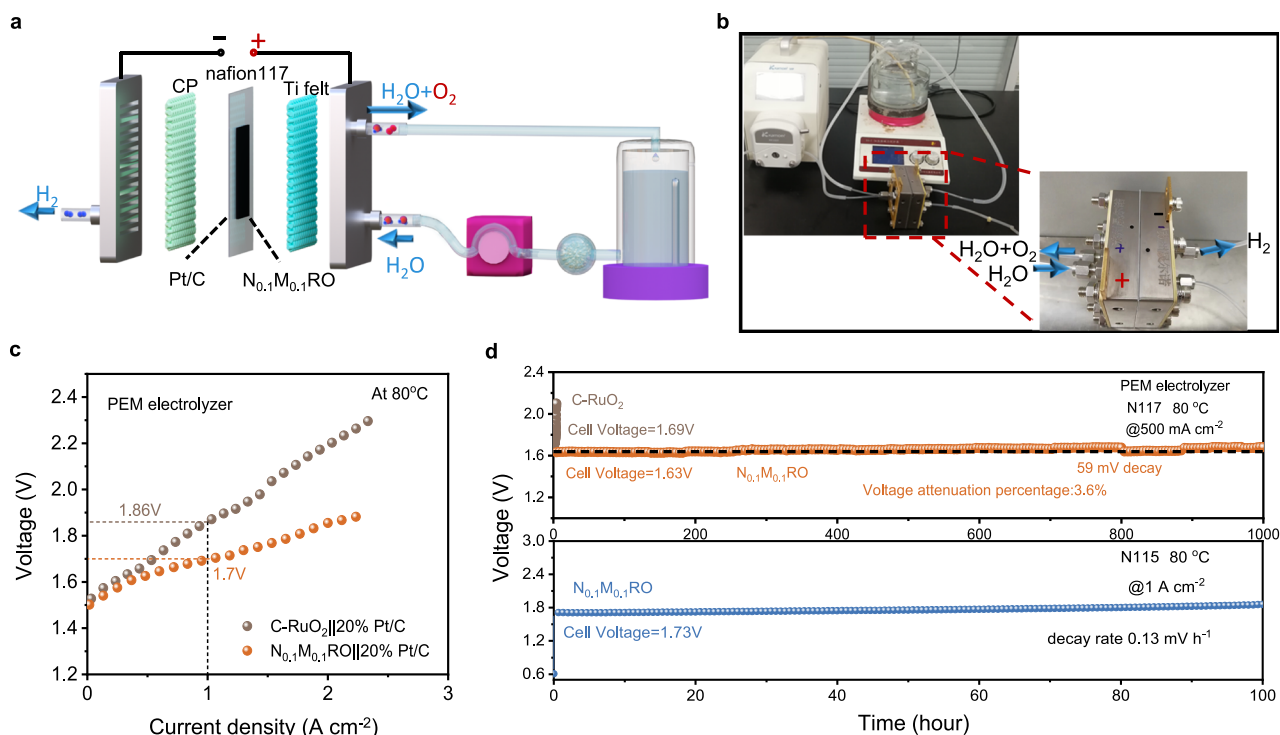


**Fig. 6 | Overall water splitting PEM electrolyzer using  $N_{0.1}M_{0.1}RO$  as the anode catalyst in pure water at 80 °C. a, b** Schematic diagram (a) and photograph (b) of the PEM electrolyzer device. **c** Steady-state polarization curves collected from the

PEM electrolyzer utilizing  $N_{0.1}M_{0.1}RO$  or C-RuO<sub>2</sub> as an anode catalyst and 20 wt% Pt/C as a cathode catalyst. **d** Chronopotentiometry curve of the PEM electrolyzer under 500  $mA\ cm^{-2}$  (top) and 1  $A\ cm^{-2}$  (bottom).

MnO<sub>x</sub> groups reached dynamic equilibrium and their coordination numbers remained relatively constant (Fig. 5g and Supplementary Table 2). The unchanged first Ru-O shell after a long time at high current stability suggests the robust stability of  $N_{0.1}M_{0.1}RO$  catalyst during acidic OER measurement. Additionally, the Mn K-edge and Nb K-edge EXAFS spectra with the first M-O shell for  $N_{0.1}M_{0.1}RO$  150 h@200  $mA\ cm^{-2}$  demonstrate a similar profile to the Ru K-edge EXAFS (Fig. 5f), evidencing that Nb and Mn are stable in RuO<sub>2</sub> matrix and no impurities are formed, without segregation. It is noted that the Mn-O and Nb-O bond length in  $N_{0.1}M_{0.1}RO$  150 h@200  $mA\ cm^{-2}$  shortens by 0.011 Å and 0.031 Å compared to that of original one, respectively. However, negligible change is observed on Ru-O bond length (Supplementary Fig. 47). As a result, the oxidation behavior of Nb and Mn ions during the long-term acidic OER reaction strengthens bond between Nb/Mn and O, giving rise to shorting the second scattering path. Therefore, the difference in Ru-O, Mn-O, and Nb-O bond length can increase the electron density around Ru sites, which is beneficial to stabilize RuO<sub>2</sub> and protects Ru sites from over-oxidation during OER catalysis at high current density. O K-Edge XAS spectra shows that there is no change in the fission energy value of 10Dq and  $I_{eg}/I_{2g}$  ratio (Supplementary Fig. 48 and Supplementary Table 10), indicating the maintained crystal structure and absence of oxygen vacancy. As a result, the  $N_{0.1}M_{0.1}RO$  electrode demonstrates a superior stability for acidic OER under 200  $mA\ cm^{-2}$  for 400 h with only 27 mV decay (Supplementary Fig. 49). Post-characterizations, including XRD, SEM, Raman, and EDS analysis of the  $N_{0.1}M_{0.1}RO$  catalyst evidence the unchanged morphology, stable crystal structure and elemental ratios (Supplementary Figs. 50 and 51).

### Electrocatalytic activity in a PWMWE device for overall water splitting

Given the electrocatalytic property of  $N_{0.1}M_{0.1}RO$  catalyst for acidic OER in a three-electrode system, we further evaluate its performance in a PEM electrolyzer (Fig. 6a, b) by applying Pt/C (20 wt%) as the

cathode catalyst. A membrane electrode assembly (MEA) was prepared by catalyst coated film (CCM) method through spraying catalyst ink onto the  $2 \times 2\ cm^2$  Nafion 117 membrane with a mass loading of 2  $mg_{cat}\ cm^{-2}$  (see Methods for details). The steady-state polarization curves operated at 80 °C (Fig. 6c) show that the cell voltage required to reach a current density of 1  $A\ cm^{-2}$  and 2  $A\ cm^{-2}$  in  $N_{0.1}M_{0.1}RO$ ||20% Pt/C electrolyzer is 1.70 V and 1.85 V, respectively, which is much lower compared with C-RuO<sub>2</sub>||20% Pt/C electrolyzer (1.86 V and 2.20 V). Notably, the energy efficiency of the PEM electrolyzer reaches to 72.4% under 1  $A\ cm^{-2}$  (see Supplementary Note I). Moreover, the PEM electrolyzer using  $N_{0.1}M_{0.1}RO$  catalyst could be operated at 0.5  $A\ cm^{-2}$  for at least 1000 h with the cell voltage and attenuation rate of 1.63 V and 3.6%, respectively (Fig. 6d). By contrast, the PEM electrolyzer using C-RuO<sub>2</sub> as anode catalyst shows an obvious decay of 0.2 V after only 3.6-h continuous operation at 0.5  $A\ cm^{-2}$ . Even if we assume that all Ru sites in the  $N_{0.1}M_{0.1}RO$  nanocatalyst are active for the OER, the lower bound estimated turnover frequency (TOF) of  $N_{0.1}M_{0.1}RO$  is 0.41  $O_2\ s^{-1}$  at 0.5  $A\ cm^{-2}$ , which is higher than that of C-RuO<sub>2</sub> (0.34  $O_2\ s^{-1}$ , Supplementary Table II). The real TOF value should be much higher than the theoretical value since the calculations assumed all the Ru sites (even buried inside) as active sites for OER. When we assume only the surface Ru sites (estimated around 1.93%, Supplementary Table II, using reported method<sup>4</sup>) are active towards OER, the TOF of  $N_{0.1}M_{0.1}RO$  can be estimated as 21.2  $O_2\ s^{-1}$ . Moreover, the corresponding energy consumption of this PEM electrolyzer operated at 0.5  $A\ cm^{-2}$  is 43.68 kWh for 1 kg  $H_2$  (see details in Supplementary Note I), less than the International Renewable Energy Agency's goal of achieving an electrical efficiency of <45 kWh for 1 kg  $H_2$  by 2050. According to the calculation procedure from the US DOE<sup>53</sup>, the estimated cost of 1 kg of hydrogen produced by this PEM electrolyzer is about US\$0.99 (make up the energy consumption of 6 kWh  $kg_{H_2}^{-1}$ ), which is lower than the DOE target of US\$2 per kg of  $H_2$ . Subsequently, we proceeded to apply the as-prepared  $N_{0.1}M_{0.1}RO$  in a PEM electrolyzer (anode) with a higher current density of 1  $A\ cm^{-2}$ . Notably, the cell

voltage can be maintained over 100 h of electrolysis with 13 mV decay, implying the potential of using  $\text{Nb}_{0.1}\text{Mn}_{0.1}\text{RuO}_2$  catalyst for practical application (Fig. 6d). This PEM electrolyzer demonstrates the superior operation durability for  $\text{H}_2$  evolution, outperforming most of reported devices fabricated with Ru-based catalysts and even Ir-based catalysts (Supplementary Table 12).

In summary, we propose a synergistic complementary co-doping strategy to design a  $\text{RuO}_2$  based OER catalyst with high activity and stability, enabling operation of PEMWE device at current density  $>0.5 \text{ A cm}^{-2}$  for  $>1000 \text{ h}$ . Detailed XAS analysis on metal and oxygen elements demonstrate that the fluctuation of valence state of Nb and Mn atoms in  $\text{RuO}_2$  and the charge redistribution effect in Ru-O-Nb/Mn structural motif can dynamically tailor the charge of Ru site, preventing the overoxidation of Ru site to  $4+$  during OER. Theoretical calculations further demonstrate that the co-substitution of Nb and Mn can stabilize the lattice oxygen and surface Ru site by increasing the formation energy. The PEMWE device assembled with  $\text{Nb}_{0.1}\text{Mn}_{0.1}\text{RuO}_2$  as OER catalyst can be stably operated for 1000 h at  $0.5 \text{ A cm}^{-2}$  with a small decay rate of  $59 \mu\text{V h}^{-1}$ , outperforming the reported benchmarks. This work offers insight for rational catalyst design for practical, cost-effective, and highly efficient PEM water electrolyzer.

## Methods

### Chemicals and materials

Ruthenium chloride hydrate ( $\text{RuCl}_3 \cdot 3\text{H}_2\text{O}$ , 99.9%), niobium chloride ( $\text{NbCl}_5$ , 99.9%), manganese dichloride hydrate ( $\text{MnCl}_2 \cdot 4\text{H}_2\text{O}$ , 99.9%), commercial rutile-type  $\text{RuO}_2$  (99.9%), and poly (vinyl pyrrolidone) (PVP, 99.9%) were all purchased from Aladdin Biological Technology Co., Ltd. Ethanol (99.9%), and 5 wt% Nafion solution were purchased from Sigma-Aldrich. The carbon fiber paper (TGP-H-060) was purchased from Toray Industries, Inc. All chemicals were used as received without any further purification. The utilized aqueous solutions were prepared using deionized water with a resistivity of  $18.2 \text{ M}\Omega \text{ cm}^{-1}$ .

### Synthesis of $\text{Nb}_x\text{Mn}_{0.2-x}\text{Ru}_{0.8}\text{O}_2$ nanoparticles

The traditional sol-gel method was used to synthesize the catalyst under an ambient condition. First, 0.025 mmol  $\text{NbCl}_5$ , 0.025 mmol  $\text{MnCl}_2 \cdot 4\text{H}_2\text{O}$  and 0.2 mmol  $\text{RuCl}_3 \cdot 3\text{H}_2\text{O}$  were dissolved in 10 mL ethanol, respectively, and mixed in a 20 mL reaction flask to avoid the hydrolysis of metal precursors. The resulting maroon homogeneous solution was then sonicated for 10 min, followed by the addition of 60 mg PVP to the mixture to obtain a light-yellow suspension. Next, the sealed vial is transferred to the oil bath and stirred at  $80^\circ\text{C}$  for 6 h. Then, the bottle cap is opened to evaporate all the ethanol solvent, obtaining a yellow-green powder precursor. Finally, the obtained precursors were transferred to a porcelain boat and annealed in an air atmosphere for 3 h in a tube furnace at  $400^\circ\text{C}$  at a ramp rate of  $5^\circ\text{C min}^{-1}$ . The collected black product is labeled  $\text{Nb}_{0.1}\text{Mn}_{0.1}\text{Ru}_{0.8}\text{O}_2$  ( $\text{Nb}_{0.1}\text{Mn}_{0.1}\text{RO}$ ). Home-made  $\text{RuO}_2$  (HM- $\text{RuO}_2$ ),  $\text{Nb}_{0.2}\text{Ru}_{0.8}\text{O}_2$  (NRO),  $\text{Mn}_{0.2}\text{Ru}_{0.8}\text{O}_2$  (MRO), and  $\text{N}_x\text{Mn}_{0.2-x}\text{RuO}_2$  (where  $x$  represents the doping amount of Nb,  $x = 0.05, 0.07, 0.13$ , and  $0.15$ ) were prepared by the same synthesis method under different Ru/Nb/Mn feeding ratios.

### Electrochemical measurements

Electrochemical measurements were performed using an electrochemical workstation (Model CHI660E, CH instrument) and a standard three-electrode electrochemical cell. The catalytic activity of the samples was recorded in  $0.5 \text{ M H}_2\text{SO}_4$  solution ( $\text{pH} = 0.22 \pm 0.04$ ) using prepared or commercial samples, platinum sheets, and Ag/AgCl (saturated KCl) as working electrodes, counter electrodes, and reference electrodes, respectively. The reference electrode was calibrated in hydrogen-saturated  $0.5 \text{ M H}_2\text{SO}_4$ . The calibrated value for Ag/AgCl in saturated KCl was equal to 0.188 (close to the theoretical value of 0.197). All potentials were referenced to RHE via the following equation  $[E (\text{V vs. RHE}) = 0.188 + 0.059 \times \text{pH}]$ . And all polarization curves

were corrected for  $iR$  compensation within the cell. The catalyst ink is prepared by dissolving 5 mg of as prepared or commercial catalyst into a solution containing 980  $\mu\text{L}$  of ethanol and 20  $\mu\text{L}$  of 5 wt% Nafion solution. In order to compare the OER activity of  $\text{N}_x\text{Mn}_{0.2-x}\text{RuO}_2$  and C- $\text{RuO}_2$ , 1 mL of as-prepared ink was dropped on a carbon fiber paper within a  $1 \text{ cm}^2$  area for the above three-electrode test. The mass loading of catalysts is weighed and calculated as  $3 \text{ mg cm}^{-2}$ . LSV curves are scanned  $\text{N}_x\text{Mn}_{0.2-x}\text{RuO}_2$  and C- $\text{RuO}_2$  in  $0.8\text{--}1.8 \text{ V vs. Ag/AgCl}$  voltage window with  $0.5 \text{ M H}_2\text{SO}_4$  as electrolyte and a scanning rate of  $5 \text{ mV s}^{-1}$ . Considering that the attenuation rate in OER testing is strongly influenced by various factors, including catalyst layer quality, active site blockage by microbubbles, and changes in surface oxidation state<sup>54,55</sup>. For large-scale preselection of promising catalyst designs, it remains important to use RDE technology to rapidly characterize new catalysts prepared from milligram quantities of materials<sup>56</sup>. For the mass loading of catalysts is weighed and calculated as  $0.4 \text{ mg cm}^{-2}$ , 20  $\mu\text{L}$  of prepared ink was dropped onto the rotation disc electrode within a  $0.2475 \text{ cm}^2$  area for the above three-electrode test. All polarization curves were corrected by ohmic potential drop ( $iR$ ) caused by the electrolyte/contact resistance of the setup. The Ohmic loss is corrected by subtracting the ohmic voltage drop from the measured potential, so the  $iR$ -corrected potential is expressed as  $E - 90\% iR_s$  (where  $i$  is the current and  $R_s$  is the series resistance during the OER test)<sup>20,24</sup>. The ohmic resistance is determined at high frequencies using electrochemical impedance spectroscopy (EIS). Chronopotentiometry tests were carried out in  $0.5 \text{ M H}_2\text{SO}_4$  electrolyte, platinum sheet as cathode and OER catalyst dropped on Ti mesh (the mass loading of catalysts is weighed and calculated as  $0.4 \text{ mg cm}^{-2}$ ) or carbon fiber paper (the mass loading of catalysts is weighed and calculated as  $3 \text{ mg cm}^{-2}$ ) as anode in a two-electrode system with current density of  $10 \text{ mA cm}^{-2}$  or  $200 \text{ mA cm}^{-2}$ , respectively. The data obtained from CP stability tests were not  $iR$  corrected and displayed as raw data. The Tafel slopes were derived from LSV curves at a low overpotential fitted to the Tafel Eq. (1):

$$\eta = a + b \log j \quad (1)$$

where  $\eta$  is the overpotential,  $a$  is the constant,  $b$  is the Tafel slope, and  $j$  is the current density.

### ICP analysis of the Ru/Nb/Mn dissolution

The dissolution of catalysts during the OER process at 100 or  $200 \text{ mA cm}^{-2}$  in a total volume of 50 mL electrolyte was quantified by inductively coupled plasma optical emission spectrometry (ICP-OES, iCAP7400, Thermo Fisher). A volume (10 mL) of electrolyte was used to fulfill the limit of detection of the equipment. The electrolyte for  $\text{Nb}_{0.1}\text{Mn}_{0.1}\text{RO}$  was sampled after 400 h electrolysis, for NRO was sampled after 106.8 h electrolysis, for MRO was sampled after 171.6 h electrolysis, for HM- $\text{RuO}_2$  was sampled after 38.4 h electrolysis, while the electrolyte for C- $\text{RuO}_2$  was sampled after 9.58 h electrolysis.

### PEM electrolyzer test

The anode catalyst for preparing the MEA was  $\text{Nb}_{0.1}\text{Mn}_{0.1}\text{RO}$  or C- $\text{RuO}_2$ , and the cathode catalyst was commercial Pt/C (20% wt%) by the catalyst-coated membrane method with a geometric area of  $2 \times 2 \text{ cm}$  ( $4 \text{ cm}^2$ ). Firstly, A Nafion 117 membrane was sequentially washed by 5 wt%  $\text{H}_2\text{O}_2$ ,  $0.5 \text{ M H}_2\text{SO}_4$ , and deionized water at  $80^\circ\text{C}$  for 1, 1, and 0.5 h, respectively. After the above steps are completed, the membrane is stored in  $0.5 \text{ M H}_2\text{SO}_4$  electrolyte. Then, the anode catalyst was dispersed in a mixture of isopropyl alcohol and Nafion solution with the amount of 20 wt% for ionomer. For the cathode, the Pt/C electrocatalyst was suspended in a mixture of isopropanol, distilled water, and Nafion solution with the amount of 40 wt% for ionomer. The ink was ultrasonically homogenized and sprayed onto two sides of Nafion 117 film at  $120^\circ\text{C}$ . The mass loads of anode and cathode

catalysts were controlled at  $2 \text{ mg}_{\text{cat}} \text{ cm}^{-2}$  and  $0.4 \text{ mg}_{\text{Pt}} \text{ cm}^{-2}$ , respectively. Finally, the device is integrated by pressing the cathodic diffusion layer, CCM, PTL, and two Ti end plates with flow fields together (Fig. 6a). The area covered by the serpentine channel, that is the active area, is  $4 \text{ cm}^2$ . The PEM electrolyzers were operated at  $80^\circ\text{C}$  with distilled water as reactant under a flow rate of  $30 \text{ mL min}^{-1}$ . Before the polarization test, the cell was activated at  $1 \text{ A cm}^{-2}$  for 1 h. The steady-state polarization curve was acquired under a galvanostatic mode of 0 to  $4 \text{ A cm}^{-2}$ . Stability of PEM electrolyzer measured at  $500 \text{ mA cm}^{-2}$ . All data of PEM electrolyzer has not been *iR* corrected and displayed as raw data.

### Material characterizations

Powder X-ray diffraction patterns of different  $\text{N}_x\text{M}_{0.2-x}\text{RO}$  samples were collected using an X-ray diffractometer (Shimadzu6000) equipped with Cu K $\alpha$  radiation ( $k = 1.5418 \text{ \AA}$ ). The size and morphology of the  $\text{N}_x\text{M}_{0.2-x}\text{RO}$  samples were characterized using a transmission electron microscope (TEM, JEM-2100). HR-TEM was performed on a double aberration-corrected FEI Titan3 80–300 Schottky FEG-TEM (field emission gun transmission electron microscope) operating at 300 kV. The corresponding elemental mappings of energy-dispersive X-ray spectroscopy (EDX) were obtained using an energy-dispersive spectrometer (Oxford). XPS measurements were conducted on an X-ray photoelectron spectrometer (Thermo Electron ESCALAB250). Due to the overlap between the Cls peak and the Ru 3d peak, we added sodium chloride solid powder as the internal standard substance to the catalyst, which was corrected indirectly by sodium and chlorine elements. X-ray absorption spectra (XAS) were collected at Beamline 14 W at Shanghai Synchrotron Radiation Facility (SSRF). The as-prepared sample powder (40 mg) was directly coated on the adhesive tape (Scotch Magic Tape,  $1 \times 0.5 \text{ cm}^2$ ) for the XAS collection. As for ex-situ characterizations on  $\text{N}_{0.1}\text{M}_{0.1}\text{RO}$   $50 \text{ h@}10 \text{ mA cm}^{-2}$  and  $\text{N}_{0.1}\text{M}_{0.1}\text{RO}$   $150 \text{ h@}200 \text{ mA cm}^{-2}$  samples, they were directly taken out from the electrolyte after the testing and washed with ethanol several times followed by drying process under an infrared lamp for further XAS analysis. The Beijing Synchrotron Radiation Facility (BSRF) 4B9B beam provides soft X-rays with an energy range of 10–1100 eV. A branch protruding from the spherical grating is used for soft X-rays in the 62–1100 eV energy range, from which O-K-Edge XAS spectra are obtained and analyzed.

### In situ Raman characterizations

The  $\text{N}_{0.1}\text{M}_{0.1}\text{RO}$  catalyst was uniformly dispersed on carbon paper electrode as the anode, and the mass loading was  $5 \text{ mg}_{\text{cat}} \text{ cm}^{-2}$ . In addition, platinum sheet was used as the counter electrode and Ag/AgCl (saturated KCl) as the reference electrode, and they were jointly assembled in a homemade electrochemical set-up with  $0.1 \text{ M HClO}_4$  electrolyte. Raman spectra were recorded using LabRAM Aramis by applying different potentials (1.3–1.8 V vs.RHE, without *iR* correction) with 532 nm laser as excitation source.

### DEMS tests

The online DEMS system used was the QAS 100 device (Linglu Instruments, Shanghai), which was carried out in an electrochemical cell with a typical three-electrode system. As for the electrochemical system, the Ag/AgCl and Pt wire are served as reference and counter electrodes, respectively. The working electrode is a porous Au film supported on a porous polytetrafluoroethylene membrane. The catalysts ink was dropped cast onto the Au film and naturally dried. For isotope labeling measurements, 2 mL of  $0.5 \text{ M H}_2\text{SO}_4$  was prepared using  $\text{H}_2^{18}\text{O}$  (97 at. %) as solvent. First, the  $\text{N}_{0.1}\text{M}_{0.1}\text{RO}$  catalyst was performed three cycles in  $^{18}\text{O}$ -labeled  $0.5 \text{ M H}_2\text{SO}_4$  electrolyte in the potential range of 1.14 to 1.69 V versus RHE at a scan rate of  $5 \text{ mV s}^{-1}$  for isotope labeling, and the gaseous products of  $^{32}\text{O}_2$ ,  $^{34}\text{O}_2$ , and  $^{36}\text{O}_2$  signals were recorded by mass spectrometer analysis. Electrodes and cell

were then rinsed with  $^{16}\text{O}$  water for 20 min to remove any  $\text{H}_2^{18}\text{O}$  residual and scanned in a  $0.5 \text{ M H}_2\text{SO}_4$  solution of  $\text{H}_2^{16}\text{O}$  at  $5 \text{ mV s}^{-1}$  from 1.14 V to 1.79 V versus RHE. The same method is used to record gaseous products by mass spectrometry.

### Theoretical calculations

All computation studies were performed using the projector augmented wave method<sup>57</sup> as implemented in the Vienna ab initio simulation package<sup>58</sup>. The Perdew–Burke–Ernzerhof functional<sup>59</sup> for the exchange–correlation potential and an energy cut-off of 450 eV were used. Spin polarization was adopted for all calculations. To consider long-range van der Waals (vdW) interactions, the DFT-D2 method of Grimme<sup>60</sup> was employed. Atomic structures were fully released until forces on all atoms were less than  $0.02 \text{ eV \AA}^{-1}$ , the energy convergence criterion was set to  $10^{-5} \text{ eV}$ . A  $3 \times 2$  unit cell with a 6-layer thickness was employed with  $20 \text{ \AA}$  vacuum space in the *z*-direction to avoid image interactions. The bottom three layers were kept fixed while the top free layers were relaxed during geometry optimization based on the stable rutile  $\text{RuO}_2$  (110).  $3 \times 2 \times 1$  Monkhorst–Pack *k*-meshes were used to sample the Brillouin zone for geometry relaxation.

To evaluate the catalytic activity of different systems, free energy diagrams for the OER were calculated based on the computational hydrogen electrode (CHE) model reported by Nørskov et al.<sup>61</sup>, which involves four elementary reaction steps, was used to evaluate the activity of the catalyst. The Gibbs free energy change,  $\Delta E$ , of each elementary step was obtained based on the following equation, in which the contributions of zero-point energy ( $\Delta E_{\text{ZPE}}$ ) and entropy ( $T\Delta S$ ) changes were considered:

$$\Delta G = \Delta E + \Delta \text{ZPE} - T\Delta S + \Delta G_U \quad (2)$$

Where  $\Delta E$  is the calculated energy change of the intermediates, such as  $^*\text{OH}$ ,  $^*\text{O}$ , and  $^*\text{OOH}$ .  $\Delta G_U = -eU$ , with *U* representing the applied electrode potential.

The reaction free energy of equations for OER can be described as a four-electron transfer reaction pathway in acidic media based on AEM and LOM.

### Data availability

All data needed to evaluate the conclusions in the paper are presented in the paper or the Supplementary Information. Source data are provided with this paper. Extra data is available from the corresponding author upon request. Source data are provided with this paper.

### References

- Nong, H. N. et al. Key role of chemistry versus bias in electrocatalytic oxygen evolution. *Nature* **587**, 408–413 (2020).
- Chatti, M. et al. Intrinsically stable in situ generated electrocatalyst for long-term oxidation of acidic water at up to  $80^\circ\text{C}$ . *Nat. Catal.* **2**, 457–465 (2019).
- Zhang, D. et al. Construction of Zn-doped  $\text{RuO}_2$  nanowires for efficient and stable water oxidation in acidic media. *Nat. Commun.* **14**, 2517 (2023).
- Hao, S. et al. Torsion strained iridium oxide for efficient acidic water oxidation in proton exchange membrane electrolyzers. *Nat. Nanotechnol.* **16**, 1371–1377 (2021).
- Hubert, M. et al. DOE Hydrogen Program Record 24005: Clean Hydrogen Production Cost Scenarios with PEM Electrolyzer Technology. <https://www.hydrogen.energy.gov/docs/hydrogenprogramlibraries/pdfs/24005-clean-hydrogen-production-cost-pem-electrolyzer.pdf> (2024).
- U.S. DOE Hydrogen and Fuel Cell Technologies Office. Technical Targets for Proton Exchange Membrane Electrolysis. <https://www.energy.gov/eere/fuelcells/technical-targets-proton-exchange-membrane-electrolysis>.

7. IRENA. *Making the Breakthrough: Green Hydrogen Policies and Technology Costs* (International Renewable Energy Agency, Abu Dhabi, 2021).
8. Wang, Q. et al. Long-term stability challenges and opportunities in acidic oxygen evolution electrocatalysis. *Angew. Chem. Int. Ed.* **62**, 202216645 (2022).
9. Shi, X. et al. Constructing electron-regulating structure to stabilize ruthenium sites for efficient acidic water oxidation. *Mater. Today Energy* **33**, 1011087 (2023).
10. Yoon, H. et al. Perspectives on the development of highly active, stable, and cost-effective OER electrocatalysts in acid. *Battery Energy* **2**, 20230017 (2023).
11. Wu, Z. Y. et al. Non-iridium-based electrocatalyst for durable acidic oxygen evolution reaction in proton exchange membrane water electrolysis. *Nat. Mater.* **22**, 100–108 (2023).
12. Laha, S. et al. Ruthenium oxide nanosheets for enhanced oxygen evolution catalysis in acidic medium. *Adv. Energy Mater.* **9**, 1803795 (2019).
13. Kötze, R., Stucki, S., Scherson, D. & Kolb, D. M. In-situ identification of RuO<sub>4</sub> as the corrosion product during oxygen evolution on ruthenium in acid media. *J. Electroanal. Chem.* **172**, 211–219 (1984).
14. Chen, F., Wu, Z., Adler, Z. & Wang, H. Stability challenges of electrocatalytic oxygen evolution reaction: from mechanistic understanding to reactor design. *Joule* **5**, 1704–1731 (2021).
15. Zagalskaya, A. & Alexandrov, V. Role of defects in the interplay between adsorbate evolving and lattice oxygen mechanisms of the oxygen evolution reaction in RuO<sub>2</sub> and IrO<sub>2</sub>. *ACS Catal.* **10**, 3650–3657 (2020).
16. Cherevko, S. Stability and dissolution of electrocatalysts: building the bridge between model and ‘real world’ systems. *Curr. Opin. Electrochem.* **8**, 118–125 (2018).
17. Zhu, Y. et al. Boosting oxygen evolution reaction by creating both metal ion and lattice-oxygen active sites in a complex oxide. *Adv. Mater.* **32**, 1905025 (2020).
18. Li, Z. et al. Alloy-strain-output induced lattice dislocation in Ni<sub>3</sub>Fe/Ni<sub>3</sub>Fe ultrathin nanosheets for highly efficient overall water splitting. *J. Mater. Chem. A* **9**, 4036 (2021).
19. Ibrahim, K. B. et al. Facile electron transfer in atomically coupled heterointerface for accelerated oxygen evolution. *Small* **19**, 2204765 (2023).
20. Jin, H. et al. Dynamic rhenium dopant boosts ruthenium oxide for durable oxygen evolution. *Nat. Commun.* **14**, 354 (2023).
21. Deng, L. et al. Valence oscillation of Ru active sites for efficient and robust acidic water oxidation. *Adv. Mater.* **35**, 2305939 (2023).
22. Hu, S. et al. Low-dimensional electrocatalysts for acidic oxygen evolution: intrinsic activity, high current density operation, and long-term stability. *Adv. Funct. Mater.* **32**, 2201726 (2022).
23. Kim, Y. J. et al. Highly efficient oxygen evolution reaction via facile bubble transport realized by three-dimensionally stack-printed catalysts. *Nat. Commun.* **11**, 4921 (2020).
24. Liu, H. et al. Eliminating over-oxidation of ruthenium oxides by niobium for highly stable electrocatalytic oxygen evolution in acidic media. *Joule* **7**, 558–573 (2023).
25. Qiu, L., Zheng, G., He, Y., Lei, L. & Zhang, X. Ultra-small Sn-RuO<sub>2</sub> nanoparticles supported on N-doped carbon polyhedra for highly active and durable oxygen evolution reaction in acidic media. *Chem. Eng. J.* **409**, 128155 (2021).
26. Li, L. et al. Spin-polarization strategy for enhanced acidic oxygen evolution activity. *Adv. Mater.* **35**, 2302966 (2023).
27. Wang, Y. et al. Unraveling oxygen vacancy site mechanism of Rh-doped RuO<sub>2</sub> catalyst for long-lasting acidic water oxidation. *Nat. Commun.* **14**, 1412 (2023).
28. Mizutani, U. Hume-Rothery rules for structurally complex alloy phases. *MRS Bull.* **37**, 169 (2012).
29. Wang, Z. et al. Atomic-size effect and solid solubility of multi-component alloys. *Scr. Mater.* **94**, 28–31 (2015).
30. Li, K. & Xue, D. Estimation of electronegativity values of elements in different valence states. *J. Phys. Chem. A* **110**, 11332–11337 (2006).
31. Chen, S. et al. Mn-doped RuO<sub>2</sub> nanocrystals as highly active electrocatalysts for enhanced oxygen evolution in acidic media. *ACS Catal.* **10**, 1152–1160 (2020).
32. Meng, L. et al. Raman spectroscopy analysis of magnetron sputtered RuO<sub>2</sub> thin films. *Thin Solid Films* **442**, 93–97 (2003).
33. Liang, S. et al. Ion-Sieve-confined synthesis of size-tunable Ru for electrochemical hydrogen evolution. *Nano Lett.* **24**, 757–763 (2024).
34. Huang, L. et al. NbO<sub>2</sub> electrocatalyst toward 32% faradaic efficiency for N<sub>2</sub> fixation. *Small Methods* **3**, 1800386 (2019).
35. Sardar, K. et al. Water-splitting electrocatalysis in acid conditions using ruthenate-iridate pyrochlores. *Angew. Chem., Int. Ed.* **53**, 10960 (2014).
36. Kim, J. et al. High-performance pyrochlore-type yttrium ruthenate electrocatalyst for oxygen evolution reaction in acidic media. *J. Am. Chem. Soc.* **139**, 12076–12083 (2017).
37. Li, J. et al. Structural and optical interplay of palladium-modified TiO<sub>2</sub> nanoheterostructure. *J. Phys. Chem. C* **119**, 2222–2230 (2015).
38. Soriano, L. et al. Chemical changes induced by sputtering in TiO<sub>2</sub> and some selected titanates as observed by X-ray absorption spectroscopy. *Surf. Sci.* **290**, 427–435 (1993).
39. Lusvardi, V. S. et al. An NEXAFS investigation of the reduction and reoxidation of TiO<sub>2</sub>(001). *Surf. Sci.* **397**, 237–250 (1998).
40. Yan, W. et al. Oxygen vacancy effect on room temperature ferromagnetism of rutile Co: TiO<sub>2</sub> thin films. *Appl. Phys. Lett.* **94**, 042508 (2009).
41. Van Aken, P. A., Liebscher, B. & Styrsky, V. J. Core level electron energy-loss spectra of minerals: pre-edge fine structures at the oxygen K-edge. *Phys. Chem. Miner.* **25**, 494–498 (1998).
42. Shannon, R. D. Revised effective ionic radii and systematic studies of interatomic distances in halides and chalcogenides. *Acta Crystallogr. A* **32**, 751–767 (1976).
43. Frydendal, R. et al. Benchmarking the stability of oxygen evolution reaction catalysts: the importance of monitoring mass losses. *ChemElectroChem* **1**, 2075–2081 (2014).
44. Song, J. et al. A review on fundamentals for designing oxygen evolution electrocatalysts. *Chem. Soc. Rev.* **49**, 2196–2214 (2020).
45. Zhang, N. & Chai, Y. Lattice oxygen redox chemistry in solid-state electrocatalysts for water oxidation. *Energy Environ. Sci.* **14**, 4647–4671 (2021).
46. Jo, H. C. et al. In situ Raman spectroscopy of RuO<sub>2</sub>·xH<sub>2</sub>O. *Electrochem. Solid State Lett.* **8**, 39–41 (2008).
47. Zhu, H. et al. High-entropy alloy stabilized active Ir for highly efficient acidic oxygen evolution. *Chem. Eng. J.* **431**, 133251 (2022).
48. Wang, H. et al. In situ spectroscopic identification of μ-OO bridging on spinel Co<sub>3</sub>O<sub>4</sub> water oxidation electrocatalyst. *J. Phys. Chem. Lett.* **7**, 4847–4853 (2016).
49. Wohlfahrt-Mehrens, M. & Heitbaum, J. Oxygen evolution on Ru and RuO<sub>2</sub> electrodes studied using isotope labelling and on-line mass spectrometry. *J. Electroanal. Chem.* **237**, 251–260 (1987).
50. Pauling, L. The nature of the chemical bond. III. The transition from one extreme bond type to another. *J. Am. Chem. Soc.* **54**, 988–1003 (1932).
51. Moltved, K. A. & Keep, K. P. The chemical bond between transition metals and oxygen: electronegativity, d-Orbital effects, and oxophilicity as descriptors of metal–oxygen interactions. *J. Phys. Chem. C* **123**, 18432–18444 (2019).
52. Morgan, D. J. Resolving ruthenium: XPS studies of common ruthenium materials. *Surf. Interface Anal.* **47**, 1072–1079 (2015).

53. Bender, G. & Dinh, H. *HydroGEN: Low-Temperature Electrolysis (LTE) and LTE/Hybrid Supernode* (No. NREL/PR-5900-76549) (National Renewable Energy Lab. (NREL), Golden, CO, United States, 2020).
54. Kibsgaard, J. & Chorkendorff, I. Considerations for the scaling-up of water splitting catalysts. *Nat. Energy* **4**, 430–433 (2019).
55. Ehelebe, K., Escalera-López, D. & Cherevko, S. Limitations of aqueous model systems in the stability assessment of electrocatalysts for oxygen reactions in fuel cell and electrolyzers. *Curr. Opin. Electrochem.* **29**, 10083 (2021).
56. Lazaridis, T. et al. Capabilities and limitations of rotating disk electrodes versus membrane electrode assemblies in the investigation of electrocatalysts. *Nat. Catal.* **5**, 363–373 (2022).
57. Perdew, J. P. & Wang, Y. Accurate and simple analytic representation of the electron-gas correlation energy. *Phys. Rev. B* **45**, 13244 (1992).
58. Kresse, G. & Hafner, J. Ab initio molecular dynamics for liquid metals. *Phys. Rev. B* **47**, 558 (1993).
59. Perdew, J. P., Burke, K. & Ernzerhof, M. Generalized gradient approximation made simple. *Phys. Rev. Lett.* **77**, 3865 (1996).
60. Grimme, S. Semiempirical GGA-type density functional constructed with a long-range dispersion correction. *J. Comput. Chem.* **27**, 1787–1799 (2006).
61. Nørskov, J. K. et al. Origin of the overpotential for oxygen reduction at a fuel-cell cathode. *J. Phys. Chem. B* **108**, 17886 (2004).

## Acknowledgements

This work was supported by National Key Research and development project (2023YFB4005100, 2022YFA1504000), National Natural Science Foundation of China (No. 22179029), National Natural Science Foundation of China (No. 22479005), Fundamental Research Funds for the Central Universities (buctrc202324), Young Elite Scientists Sponsorship Program by CAST (2023QNRC001) and the Young Elite Scientists Sponsorship Program by BAST (BYESS2023093).

## Author contributions

X.-M.S. and F.-M.W. conceived and supervised this research. B.-C.Y. conducted the sample synthesis, characterizations, electrochemical measurements and analyzed the data. H.L., Q.D., and A.-Q.C. performed the DFT calculations. H.L. and S.-Y.C. assisted in the fabrication of PEM electrolyzers and tested. J.P. and Y.-M.F. assisted with the ex-situ synchrotron X-ray diffraction measurements. L.C. assisted in the analysis of X-ray adsorption spectral data. M.-G.S. and Y.K. help revise the paper. B.-

C.Y., F.-M.W., and X.-M.S. wrote the manuscript with the inputs from all authors.

## Competing interests

The authors declare no competing interests.

## Additional information

**Supplementary information** The online version contains supplementary material available at <https://doi.org/10.1038/s41467-025-59710-5>.

**Correspondence** and requests for materials should be addressed to Fengmei Wang or Xiaoming Sun.

**Peer review information** *Nature Communications* thanks the anonymous reviewers for their contribution to the peer review of this work. A peer review file is available.

**Reprints and permissions information** is available at <http://www.nature.com/reprints>

**Publisher's note** Springer Nature remains neutral with regard to jurisdictional claims in published maps and institutional affiliations.

**Open Access** This article is licensed under a Creative Commons Attribution-NonCommercial-NoDerivatives 4.0 International License, which permits any non-commercial use, sharing, distribution and reproduction in any medium or format, as long as you give appropriate credit to the original author(s) and the source, provide a link to the Creative Commons licence, and indicate if you modified the licensed material. You do not have permission under this licence to share adapted material derived from this article or parts of it. The images or other third party material in this article are included in the article's Creative Commons licence, unless indicated otherwise in a credit line to the material. If material is not included in the article's Creative Commons licence and your intended use is not permitted by statutory regulation or exceeds the permitted use, you will need to obtain permission directly from the copyright holder. To view a copy of this licence, visit <http://creativecommons.org/licenses/by-nc-nd/4.0/>.

© The Author(s) 2025